Highly Forbidden Transitions in Alkalis: Preparations for a Parity Violation Experiment

by

Claudia Oliveira

A Thesis Submitted to the Faculty of Graduate Studies of
the University of Manitoba
in partial fulfillment of the requirements of the degree of

MASTER OF SCIENCE

Department of Physics and Astronomy
University of Manitoba
Winnipeg, Manitoba

ABSTRACT

Preparatory steps for the experimental investigation of the highly forbidden $5s \rightarrow 6s$ transition in rubidium using an atom trap and laser cooling are reported. A magneto-optical trap (MOT) has been assembled including saturation spectroscopy and a dichroic vapor laser lock. A frequency-doubled diode laser system has been installed to perform the spectroscopy of the forbidden transition with cold Rb atoms in the trap. The properties of the $ns \rightarrow n's$ transition in the presence of an external electric field have been investigated theoretically. A first measurement will be exploring the Stark-induced transition amplitude and the very faint magnetic dipole amplitude. The rubidium experiment is a precursor study for a long-term project at TRIUMF, Canada's National Laboratory for nuclear and particle physics, to measure atomic parity violation in the equivalent $7s \rightarrow 8s$ transition in francium, the heaviest alkali atom which has no stable isotopes.

TABLE OF CONTENTS

LIST OF TABLES

LIST OF FIGURES

Chapter 1

INTRODUCTION

This thesis presents preparatory work towards a long-term program of measuring weak interaction physics in the radioactive atom of francium at TRIUMF, Canada's National Laboratory for nuclear and particle physics in Vancouver. The intention is to measure an effect known as atomic parity nonconservation (or atomic parity violation, the two terms will be used interchangeably) in the francium atom, where the effect is, due to the large nuclear charge of $Z = 87$, about 18 times larger than in cesium, where so far the most precise experiments have been carried out. A major complication is that francium possesses no stable isotopes, so it must be produced in a nuclear reaction on-line at an accelerator. Due to the low production rates for radioactive species (relative to the availability of stable isotopes), the atomic spectroscopy has to be carried out extremely efficiently. We plan to employ laser cooling and atom trapping techniques for this purpose.

To explore techniques, we are in the process of setting up an off-line experiment with stable rubidium at the University of Manitoba. This thesis presents the first steps: The construction of a magneto-optic trap for the capture and storage of a cold ($\approx 100\mu$K) sample of rubidium atoms. Once this basic facility is running, it will be used to perform spectroscopy on the $5s \rightarrow 6s$ transition in Rb, the equivalent transition to $6s \rightarrow 7s$ in Cs, where the atomic parity violation work has been carried out, and to $7s \rightarrow 8s$ in francium. A frequency-doubled diode laser system is available for this purpose and has been tuned to the correct wavelength at 496 nm to excite

$5s \rightarrow 6s$.

In addition, we look into the theory of the $5s \rightarrow 6s$ transition in the presence of an external electric field (which plays a pivotal role in a parity violation experiment in Cs and Fr), including a Stark-induced electric dipole amplitude, a magnetic dipole amplitude, which by itself is very interesting to study in Rb and other alkalis [1] , and the weak interaction induced electric dipole amplitude and their interference. A program has been developed to calculate transition rates for different geometries for the external fields and laser polarizations.

1.1 Towards an APNC measurement in Fr

The APNC effect in francium is about 18 times larger than in cesium, which was the atom used in the best experiments about non-conservation of parity. Later it will be explained why the size of the APNC effect increases with the atomic number, being this one of the reasons for Fr to be a good candidate for an APNC experiment, and also because of the simplicity of alkali's atomic structure compared to other atoms that have more than one electron in their outer shells.

As a means to gain expertise towards APNC experiments using Fr, basic spectroscopy has to be carried out on the weak 5s $\rightarrow$ 6s transition in Rb. A frequency-doubled diode laser system, wavelength tuned to 496 nm, has been installed and is being readied to excite the transition of the Rb atoms in a magneto-optical trap. It is not possible to use Fr vapor cells because macroscopic quantities of this atom are not available, but it is possible to laser trap, and bring them to a similar density as another stable alkali. The knowledge acquired using a trap-based scheme for Rb can be later used to implement an on-line experiment with Fr.

1.1.1 Overview of APNC Experiments and Search for Physics Beyond the SM

Before 1956 it was believed that all fundamental interactions would be indistinguishable from its mirror image, until the proposition that parity might not be conserved in weak interactions was raised by Lee, T.D. and Yang, C.N. [2], and in the next year experimentally proven [3] [4] [5]. Yakov Borisovich Zel'dovich was the first to propose that parity non-conservation is induced by weak neutral currents, in 1959 [6], but due to the weakness of the effect he concluded that it could not be observed. In 1974, M. A. Bouchiat and C. Bouchiat, arrived at the conclusion that the parity non-conserving effect was increased with the atomic number Z, about Z^3, and for the first time the violation of parity was sufficiently large to be measured, and then APNC experiments were done with some heavy atoms. The Paris group measured the first APNC effect in Cs atoms with 20% of accuracy, what was later improved to 12%. Subsequently the Boulder group achieved an accuracy of 2%.

The search for new physics by means of APNC is done by comparing the basic standard model predictions to the estimated parity values derived from the experiments. The higher the atomic number, the larger the APNC effect, which limits the choice of atom to the heavy ones. But rather than that it is also necessary to have a very good knowledge of the atomic structure in order to predict the APNC values with accuracy, explaining why cesium ($Z = 55$) was the most used atom for these experiments. With modern laser-cooling techniques and better ways to store highly radioactive atoms like francium ($Z = 87$), it is possible to obtain larger APNC effects.

1.1.2 Other APNC Experiments, Current State

After the Bouchiats' observation that the parity non-conservation effect is intensified approximately proportional to the cube of the atomic number, suggesting it could be detectable if tested on heavy atoms, the long search for the APNC phenomenon started.

The first experiment to point at the existence of neutral weak currents was made in 1978 in Novosibirsk, by Barkov and Zolotorev [7]. They used the optical rotation technique in bismuth atoms, obtaining results that agreed with the Weinberg-Salam model. This technique consists of measuring the rotation of the light beam after passing through a medium that is under application of a longitudinal magnetic field. It takes advantage of the fact that the refractive index of the medium is not the same for right and left circular polarized components of the light, leading to different phase shifts and therefore polarizing the beam by an angle φ proportional to,

$$R(\varphi) = \frac{Im(E1_{pnc})}{M1} \tag{1.1}$$

where E1 is the electric dipole, and M1 the magnetic dipole transition matrix element.

In the next year the Berkeley group observed the APNC effect in thallium using the Stark-interference method [8], suggested by Bouchiat [9]. It consists of measuring the Stark mixing parameter β, which originates from the interference between the parity-violation induced E1 and the Stark induced E1 amplitudes, determining the transition rate

$$R_{Stark} = \frac{Im(E1_{pnc})}{\beta}. \tag{1.2}$$

The results obtained by the Novosibirsk and Berkeley groups helped to confirm weak neutral currents do exist, and that parity is violated in the neutral current as predicted by the standard model.

The parity non-conservation measurements made by Boulder, Oxford, Paris, and Seattle groups between 1980 and 1995 with Bi, Cs, Pb, and Tl, reached an accuracy of about 1-2%. In 1997, the Boulder group improved the accuracy to 0.35%, and extracted the first measurement of anapole moment using atoms of ^{133}Cs [10].

Currently, several efforts are in progress. The Berkeley ytterbium is the only one which has observed a parity violation signal so far. These experiments will be briefly introduced in the following:

Berkeley, Budker group

Recently, researchers in the Budker group at the University of California at Berkeley, have found, in the $6s^2\ ^1S_0 \rightarrow 5d6s\ ^3D_1$ forbidden transition of ytterbium the largest APNC effect yet observed [11]. The parity forbidden effect measured on ^{174}Yb was 100 times larger than in ^{133}Cs. The main objectives of the group are the measurements of the changes in the weak charge in each one of the 7 isotopes of ytterbium, the study of the nuclear structure by exploring the arrangement of the neutrons in heavy atoms, whether they surround the nucleus forming a outer layer covering the protons in the center, and ultimately detect anapole moment in the outer layer of neutrons (not yet observed since this phenomenon was only measured in valence protons).

Seattle, Fortson group

This group is using a single trapped ion of barium, or radium as another alternative, to search for parity non-conservation, using a technique of spin rotation produced by an energy shift of the ion, called "light shift" [12], at the Larmor precession frequency [13]. Barium has 9 stables isotopes and its APNC effect is 2.5 times larger than in cesium atoms.

Yale, DeMille group

At Yale, this group uses diatomic molecules in the investigation of parity non-conservation and anapole moments by placing them in a strong magnetic field [14].

Legnaro, Maryland/TRIUMF groups

These groups are working towards APNC and anapole moment measurements using the heaviest alkali atom, francium, which has an effect 20 times larger than in atoms of cesium [15] [16].

1.2 Searches for Physics Beyond the SM

The search for 'new physics' beyond the Standard Model is usually associated with high energy physics experiments at large colliders such as LHC. However, low-energy measurements have historically played an important role, as well, and they still do. For example, searches for permanent electric dipole moments in atomic and subatomic particles, indicative of the violation of time reversal symmetry, are a domain of atomic physics methods; these experiments put some of the most severe constraints on extensions of the Standard Model such as supersymmetry. In high energy experiments, one strives for the direct production of new particles. These particles generally should have very large mass, otherwise they would have been discovered already (unless they were exceedingly weakly interacting with conventional matter). Therefore, low-energy approaches have to be different: Even if it is not possible energetically to produce the *real* particle, it can emerge as a *virtual* particle for a suitable short time (following the uncertainty principle) in a low-energy interaction, and with sufficiently sensitive measurement methods, the existence of a new particle/interaction can be inferred.

To make up for the drastically reduced production cross section for the virtual particle, low-energy experiments usually look for violations of 'fundamental symmetries', i.e. we look for new interactions that are not invariant under the discrete symmetries of time (T), parity (P), charge conjugation (C), or combinations thereof, and Lorentz invariance. Transformations connected with these symmetries (spatial mirror for parity, particle - antiparticle for charge conjugation, Lorentz boosts) will result in experimental signatures that clearly distinguish the new processes from the known ones.

Atomic parity nonconservation is one of several types of low-energy parity-violations experiments that search for new physics. To compare them, one can, among other choices, plot their sensitivity of determining one of the central parameters of the Standard Model, the Weinberg angle θ_W (usually given as $\sin^2\theta_W$). Figure 1.1 shows the

situation: First, the Weinberg angle is not a constant, but changes its value with the momentum transfer involved in the process under consideration; this is referred to as the 'running' of the Weinberg angle. While the very precise measurements at LEP gave an accurate value for $\sin^2\theta_W$ at 90 GeV, low-energy experiment are required to confirm this running.

APNC measures the strength of the weak neutral current at very low momentum transfer. There are three types of such "low-energy" weak neutral current measurements with complementary sensitivity. The atomic weak charge is predominantly sensitive to the neutron's weak charge, as the proton weak charge is proportional to $(1 - 4\sin^2\theta_W)$, which accidentally is near zero (see next Chapter for details on the weak charge). The Qweak electron scattering experiment on hydrogen (at Jefferson National Laboratory, Newport News, Virginia) will be sensitive to the proton's weak charge. The SLAC E158 Moeller scattering experiments (Stanford) are sensitive to the electron's weak charge. Different Standard Model extensions then contribute differently. The atomic weak charge is relatively insensitive to one-loop order corrections from all SUSY particles, so its measurement provides a benchmark for possible departures by the other low-energy observables. Moeller scattering is purely leptonic and has no sensitivity to leptoquarks, so APNC can then provide the sensitivity to those.

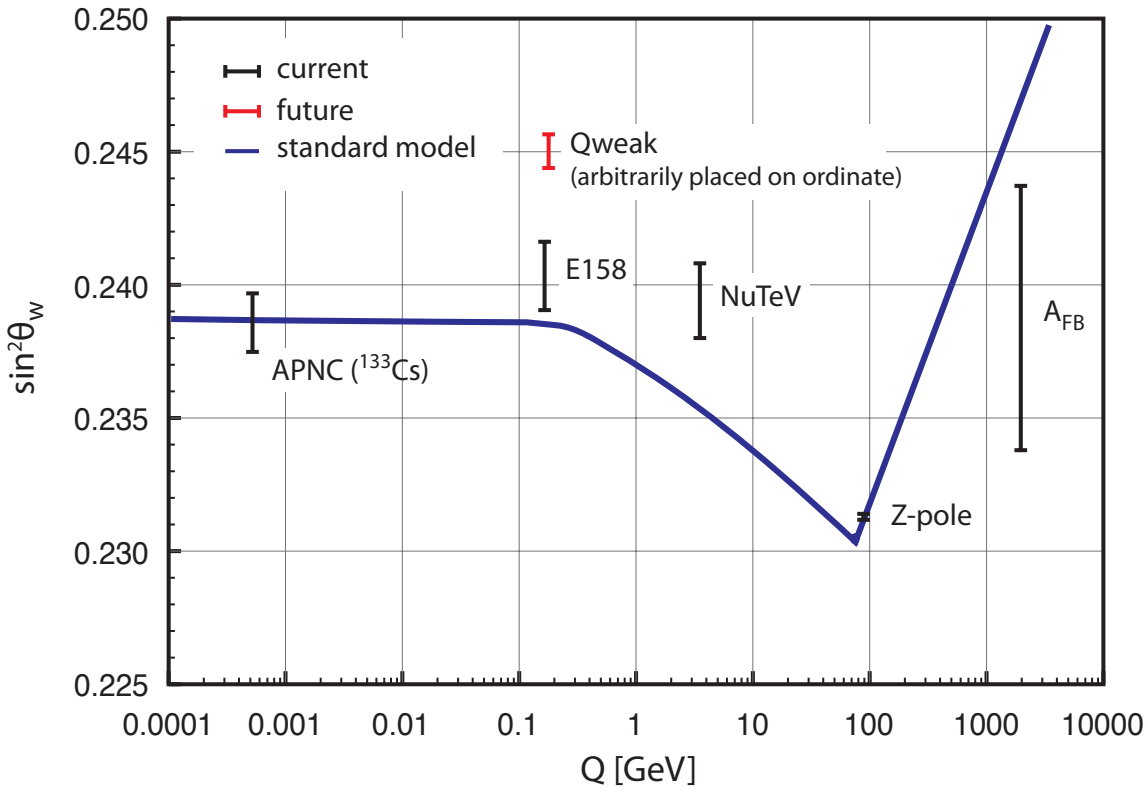

Figure 1.1: Running of the weak mixing angle

Chapter 2

COMPLETE DESCRIPTION OF THE $S \rightarrow S$ TRANSITION

Atomic parity violation arises mainly from the exchange of a heavy Z boson between the electron in the atom and the quarks in the nucleus. This weak interaction does not conserve parity but conserves time reversal, and can be dependent or independent of the nuclear spin according to whether the nucleon or the electron constitute a weak current of axial type, respectively.

According to [17] the Hamiltonian in the case of an infinitely heavy nucleon, and neglecting electromagnetic radioactive corrections, will be,

$$H = \frac{G}{\sqrt{2}}(k_{1i}\gamma_5 - k_{2i}\boldsymbol{\sigma}\cdot\boldsymbol{\alpha})\delta(\boldsymbol{r}), \tag{2.1}$$

$G = 1.027 \times 10^{-5} m_p^{-2}$ is the Fermi constant, representing the strength of the interaction, and m_p is the mass of the proton; γ_5 and $\boldsymbol{\alpha}$ are Dirac matrices, and $\boldsymbol{\sigma_n} = 2\boldsymbol{S}$ are Pauli spin matrices. The k coefficients are constants, representing the contribution given by the protons ($i = p$) or neutrons ($i = n$) in the parity violating interaction.

If the interaction is nuclear spin independent (dependent), the coupling between nucleon and electron currents is given by k_{1i} (k_{2i}). So accordingly to the electroweak theory of Glashow [4], Weimberg [3], and Salam [18], these proton and neutron constants are given by,

$$k_{1p} = \frac{1}{2}(1 - 4sin^2\theta_W) \approx 0.04 \qquad k_{1n} = -\frac{1}{2} \tag{2.2}$$

$$k_{2p} = -k_{2n} = -\frac{1}{2}(1 - 4sin^2\theta_W)\eta \approx 0.05. \tag{2.3}$$

The Weinberg angle is estimated as $sin^2(\theta_W) \approx 0.23$, and $\eta = 1.25$. Equation 2.1 can be separated into a nuclear spin dependent part, containing the k_{1i} coefficients, and a nuclear spin independent part, with the k_{2i} coefficients. The Hamiltonian of every nucleon must be added in order to obtain the total parity violating potential of the atom.

2.1 Nuclear Spin Independent Interaction

Heavy atoms, due to the coherent contribution of the nucleons, dominate this type of interaction. The Nuclear Spin Independent (nsi) potential H_{pv}^{nsi} will mix atomic levels of opposite parity, and as a result otherwise forbidden E1 transitions can be excited between states of the same parity.

The Hamiltonian for the nsi part is given by,

$$H_{pv}^{nsi} = \frac{G}{\sqrt{2}} \frac{Q_W}{2} \gamma_5 \delta(\boldsymbol{r}), \tag{2.4}$$

$$\text{Weak charge: } Q_W = 2(k_{1p}Z + k_{1n}N).$$

The Hamiltonian for nuclear spin independent interactions is proportional to the weak charge, which represents the strength of the parity-violating part of the weak force between leptons and quarks. Z gives the number of protons, and N the number of neutrons.

As it was seen before in equations 2.2 and 2.3, the k_{1n} term dominates thus,

$$Q_W = 2(k_{1p}Z + k_{1n}N) \simeq 2\left(\frac{1 - 4sin^2\theta_W}{2}Z - \frac{1}{2}N\right) \simeq -N. \tag{2.5}$$

This shows that atomic parity violation is largely sensitive to the neutrons in the nucleus. As a result, improved APNC measurements will need improved knowledge of the neutron distribution in the nucleus.

2.2 Nuclear Spin Dependent Interaction

The second part of equation 2.1 is nuclear spin dependent (*nsd*), happens only with valence nucleons, and depends less on Z because of the pairing of nucleons.

Considering the contribution of all nucleons [5], the *nsd* Hamiltonian is

$$H_{pv}^{nsd} = \frac{G}{\sqrt{2}} \frac{K\mathbf{I}\cdot\alpha}{I(I+1)} k_{2i}\delta(\mathbf{r}) \tag{2.6}$$

With $K = (I+1/2)(-1)^{I+1/2-l}$, where I is the nuclear spin, and l is the orbital angular momentum of the valence nucleon.

The valence nucleons contribute to a *nsd* force generated by the hadronic axial-vector current. This force is much smaller than the one led by the *nsi* interaction, which comes from a hadronic vector-vector current, and has a coherent contribution from all nucleons.

Parity violating weak interactions inside the nucleus induce a nuclear spin dependent moment, the anapole moment. Therefore the investigation of the anapole moment can be done through measurements of the *nsd* interaction.

2.3 Z^3 Scaling of Parity Violation

Looking back to equation 2.1, with the fifth gamma matrix expanded,

$$H = \frac{G}{2\sqrt{2}m_e c}\{\boldsymbol{\alpha}\cdot\boldsymbol{p}\delta(\boldsymbol{r})[Zk_{1p}+Nk_{1n}]+(\boldsymbol{p}-i\boldsymbol{\sigma}\times\boldsymbol{p})\cdot\delta(\boldsymbol{r})[\boldsymbol{\sigma}_p k_{2p}+\boldsymbol{\sigma}_n k_{2n}+H.c.,\} \tag{2.7}$$

where $\boldsymbol{\sigma}$ is the electron spin, $\boldsymbol{p}$ the momentum, an $\boldsymbol{r}$ the position operators.;$\boldsymbol{\sigma}_p$ and $\boldsymbol{\sigma}_n$ are the proton and neutron spin operators, respectively. And $H.c.$ stands for Hermitian conjugate. Considering only the *nsi* part, and knowing that m_e and c are equal to 1 in atomic units,

$$H_{pv}^{nsi} = \frac{G}{2\sqrt{2}m_e c}\boldsymbol{\alpha}\cdot\boldsymbol{p}\delta(\boldsymbol{r})[Zk_{1p}+Nk_{1n}] = \frac{G}{2\sqrt{2}}Q_W\boldsymbol{\sigma}\cdot\boldsymbol{p}\delta(\boldsymbol{r}). \tag{2.8}$$

This Hamiltonian will mix states of same angular momentum and opposite parities.

Let's see how the interaction for an s state atom that had some p mixed into its ground s state depends on Z, the atomic number.

$$\langle n'L'|H_{pv}^{nsi}|nL\rangle = \frac{G}{2\sqrt{2}}Q_W\langle n'L'|\boldsymbol{\sigma}\cdot\boldsymbol{p}\delta(\boldsymbol{r})|nL\rangle \propto \langle n'L'|\frac{d}{dr}|nL\rangle|_{r=0}. \tag{2.9}$$

Now one has to remember that the Z boson is very heavy, about 90 GeV, hence the weak interaction is extremely short ranged. The Z travels around $10^{-18}m$ before decaying again. Therefore, if two particles want to interact via Z-exchange, they have to come extremely close, to about 1/1000 of the size of a nucleus. In atomic parity violation, the Z-exchange is between electrons in the atom and the quarks in the nucleus. The interaction is only possible when the electron is inside the nucleus, which is possible in quantum mechanics, as the s-wave function is actually non-zero at the origin:

$$|nL\rangle = R_{nl} \propto r^L Z^{L+1/2}. \tag{2.10}$$

So, at the origin, $r = 0$, we have that L must be also equal to zero,

$$R_{n0} \propto 0^0 Z^{0+1/2} = Z^{1/2}. \tag{2.11}$$

Then, the s level wave function grows as $Z^{1/2}$ at the origin.

For L different from zero, then one must have the derivative with respect to r, then,

$$\frac{dR_{nl}}{dr} \propto Lr^{L-1}Z^{L+1/2} \tag{2.12}$$

$$\frac{dR_{n1}}{dr} \propto (1)0^{1-1}Z^{1+1/2} = Z^{3/2} \tag{2.13}$$

And then the derivative (the momentum) of the p level at the origin scales with $Z^{3/2}$. Therefore it is easy to see that the mixing will occur only between s and p wave functions, and since all the contributions will be added, we see that it is proportional to $Z^{1/2}Z^{3/2} = Z^2$. And adding the result we got from the nsi coupling constant of $-N$, and knowing that the number of neutrons in heavy atoms is proportional to the number of protons, $N \approx 1.4\,Z$, we have one more factor of Z contributing to the final

approximation to the weak matrix element of $Z^3R(Z)$. $R(Z)$ is a relativistic factor that increases with Z. Therefore, the parity violating effect increases faster than Z^3 with $\langle ns|H_{pv}^{nsi}|nL\rangle \propto Z^3R(Z)$.

2.4 Transition Amplitudes

As discussed above, the parity-violating nature of the weak electron-nucleon interaction leads to a mixing of electronic s and p states. As a result, an atomic electron nominally in an s-state has some p-wave character mixed in: $|\bar{s}\rangle = |s\rangle + \epsilon|p\rangle$ and vice versa. Without the presence of parity violation, the parity selection rules strictly forbids electric dipole (E1) transitions between states of opposite parity. Since it destroys the pure parity of states, parity violation permits E1 transitions between two states of (nominally) same parity. However, this transition would be far too weak to be detected directly. For example, the APNC-induced transition in Cs 6s - 7s, which has been used in the Boulder and Paris experiments, has an oscillator strength $f \approx 10^{-22}$,which is orders of magnitude beyond detectability (the oscillator strength is a measure of the strength of the transition, and is proportional to the transition rate; strong transitions will have f close to 1, and weak transitions will have f close to zero). The solution is to interfere the parity-violating amplitude A_{PV} with a much larger, parity-conserving amplitude A_{PC}:

$$f \propto |A_{PC} + A_{PV}|^2 = |A_{PC}|^2 + 2Re(A_{PC}A_{PV}^*) + |A_{PV}|^2. \tag{2.14}$$

By observing the interference term, which is linear in A_{PV}, one 'amplifies' the APNC signal, and it is also crucial for separating the APNC effect from much larger electromagnetic backgrounds: Performing a parity-flip (i.e. reversing the direction of externally applied fields), the interference terms changes sign, leading to a modulation of the signal strength.

Alkali $ns \rightarrow n's$ transitions are nearly ideal for this purpose. While E1 transitions are not allowed between states of same parity (ignoring small parity violation effects),

magnetic dipole (M1) transitions generally are allowed and are have oscillator strength $\approx 10^5$ times weaker than an allowed E1. For interference with A_{PV} this would be much too large, as the A_{M1}^2 terms would be too dominating. However, in alkalis, in the non-relativistic approximation, the M1 amplitude between states of different principal quantum numbers n are forbidden. Only relativistic effects and the hyperfine interaction lead to a rather weak M1 amplitude, e.g. in Cs on the order of $f \approx 10^{-13}$. This amplitude by itself is too weak for an interference experiment with A_{PV}. But early on, it was realized that an externally applied electric field would produce a Stark-induced E1 amplitude A_{Stark}, which can be *tuned* to a desirable oscillator strength by varying the applied field. For this reason, the $6s \rightarrow 7s$ transition in cesium has played a dominant role in APNC experiments.

A parity violation experiment in francium could use the analogous transition $7s \rightarrow 8s$. To explore the techniques with a stable species, we plan to investigate the $5s \rightarrow 6s$ transition in rubidium. In this section, we will look at the $ns \rightarrow (n+1)s$ transition in more detail.

2.5 Stark induced electric dipole amplitude, $E1_{Stark}$

In an unperturbed system the transition amplitude between the $ns \rightarrow (n+1)s$ states is given by the sum of the weak magnetic dipole (M1) and the even weaker electric dipole ($E1_{pnc}$) transition amplitudes. A dc electric field applied to the system causes a mixing of the s and p states (Stark effect), which together with the mixing from the parity non-conserving weak neutral current interactions perturbs the s states, and therefore we make use of the first order perturbation theory to describe the system.

$$\overline{|ns_{1/2}Fm\rangle} = |ns_{1/2}Fm\rangle + \sum_{\substack{q,J \\ F',m'}} \frac{|qP_JF'm'\rangle\langle qP_JF'm'| - e\boldsymbol{E}\cdot\boldsymbol{r}|nsFm\rangle}{E_{ns} - E_{nP_J}} \qquad (2.15)$$

The state with the bar is the one perturbed by the Stark mixing. Then with the presence of the static electric field, and an oscillating electric field (ε) from the laser

beam, can give rise to a Stark induced electric dipole transition amplitude, $E1_{Stark}$.

$$(E1^{F_2m_2}_{F_1m_1})_{Stark} = \sum_{\substack{q,J \\ F,m}} \left\{ \begin{array}{l} \frac{\langle (n+1)sF_2m_2|-e\boldsymbol{E}\cdot\boldsymbol{r}|qP_JFm\rangle\langle qP_JFm|-e\boldsymbol{\varepsilon}\cdot\boldsymbol{r}|nsF_1m_1\rangle}{E_{(n+1)s}-E_{qP_J}} + \\ \\ \frac{\langle (n+1)sF_2m_2|-e\boldsymbol{\varepsilon}\cdot\boldsymbol{r}|qP_JFm\rangle\langle qP_JFm|-e\boldsymbol{E}\cdot\boldsymbol{r}|nsF_1m_1\rangle}{E_{ns}-E_{qP_J}} \end{array} \right\} \tag{2.16}$$

$\boldsymbol{D}_{eff} = e \cdot \boldsymbol{r}$ is the effective dipole operator. According to [19] the matrix elements of the effective dipole operator can be written as,

$$\langle (n+1)s_{1/2}F_2m_2|\boldsymbol{D}_{eff}|ns_{1/2}F_1m_1\rangle = \begin{array}{l} \alpha_{(n+1),n}\boldsymbol{E}_0\delta_{F_2m_2,F_1m_1} + \\ \\ i\beta_{(n+1),n}(\boldsymbol{\sigma}\times\boldsymbol{E}_0)_{F_2m_2,F_1m_1} \end{array} \tag{2.17}$$

Then,

$$\begin{aligned} (E1^{F_2m_2}_{F_1m_1})_{Stark} &= \alpha_{(n+1),n}\boldsymbol{\varepsilon}\cdot\boldsymbol{E}_0\delta_{F_2m_2,F_1m_1} + i\beta_{(n+1),n}\boldsymbol{\varepsilon}\cdot(\boldsymbol{\sigma}\times\boldsymbol{E_0})_{F_2m_2,F_1m_1} \\ &= \alpha_{(n+1),n}\boldsymbol{E}_0\cdot\boldsymbol{\varepsilon}\delta_{F_2m_2,F_1m_1} + i\beta_{(n+1),n}(\boldsymbol{E}_0\times\boldsymbol{\varepsilon})\cdot\langle F_2m_2|\boldsymbol{\sigma}|F_1m_1\rangle, \end{aligned} \tag{2.18}$$

where α and β are the scalar and tensor electric transition polarizabilities, respectively.

$$\begin{aligned} (E1^{F_2m_2}_{F_1m_1})_{Stark} &= \alpha_{(n+1),n}\boldsymbol{\varepsilon}\cdot\boldsymbol{E}_0\delta_{F_2m_2,F_1m_1} + i\beta_{(n+1),n}(\boldsymbol{E}_0\times\boldsymbol{\varepsilon})\cdot\langle F_2m_2|\boldsymbol{\sigma}|F_1m_1\rangle \\ &= \alpha_{(n+1),n}\boldsymbol{\varepsilon}\cdot\boldsymbol{E}_0\delta_{F_2m_2,F_1m_1} + \\ &\quad i\beta_{(n+1),n}[\pm(\boldsymbol{E}_0\times\boldsymbol{\varepsilon})_xC^{F_2m_2}_{F_1m_{2\pm1}} + i(\boldsymbol{E}_0\times\boldsymbol{\varepsilon})_yC^{F_2m_2}_{F_1m_{2\pm1}} + \\ &\quad (\boldsymbol{E}_0\times\boldsymbol{\varepsilon})_zC^{F_2m_2}_{F_1m_1}]\delta_{m_2,m_1} \end{aligned} \tag{2.19}$$

The C coefficients are obtained through application of the Wigner-Eckart theorem for coupled states:

$$C^{F_2m_2}_{F_1m_{2-q}} \equiv \langle F_2m_2|\sigma_{1q}|F_1m_{2-q}\rangle \left(\frac{1}{\sqrt{2}}\right)^q, \tag{2.20}$$

where $q = m_2 - m_1$.

2.6 Magnetic dipole transition, M1

Magnetic dipole transitions between states with different principal quantum number n are forbidden by the selection rules. In the case of cesium, for example, the oscillator strength is approximately 10^{-13}.

The M1 matrix element given by:

$$W_{M1} = H_L + H_S. \tag{2.21}$$

$H_L = g_L \frac{\mu_B}{\hbar} \boldsymbol{L} \cdot \boldsymbol{\beta}$ is the Hamiltonian that contributes with angular momentum to orbital magnetism. g_L is the gyromagnetic ratio that here is equal to the ratio of the effective mass by the electron mass. Since in this case both masses are equivalent, the ratio will be equal to 1. $\boldsymbol{\beta} = \boldsymbol{k} \times \boldsymbol{\varepsilon}$ is the oscillating electromagnetic field that travels in the k direction, perpendicular to the oscillating electric field ε, from the laser beam.

$H_S = g_S \frac{\mu_B}{\hbar} \boldsymbol{S} \cdot \boldsymbol{\beta}$ is the spin Hamiltonian where $\boldsymbol{S} = \hbar\sigma/2$, and σ the Pauli matrices. g_S in this case is equal to the electron g-factor and is 2. So we have,

$$W_{M1} = \frac{\mu_B}{\hbar}(\boldsymbol{L} + 2\boldsymbol{S}) \cdot \boldsymbol{\beta} = \frac{\mu_B}{\hbar}(\boldsymbol{L} + \hbar\boldsymbol{\sigma}) \cdot \boldsymbol{\beta} \tag{2.22}$$

Considering s-states, we will have L=0, then, $W_{M1} = \mu_B(\boldsymbol{\sigma} \cdot \boldsymbol{\beta})$. Therefore the matrix element for a transition $ns \rightarrow (n+1)s$ is given by,

$$\mu_B \boldsymbol{\beta} \cdot \langle (n+1)sF_2m_2|\boldsymbol{\sigma}|nsF_1m_1\rangle. \tag{2.23}$$

We see the same matrix element presented in equation 2.19. The magnetic dipole amplitude from the $(n+1)s \rightarrow ns$ transition will be multiplied by this matrix elements, giving us:

$$\begin{aligned} M1^{F_2m_2}_{F_1m_1} &= M1\boldsymbol{\beta} \cdot \langle F_2m_2|\boldsymbol{\sigma}|F_1m_1\rangle \\ &= M1\{[\pm(\boldsymbol{k} \times \boldsymbol{\varepsilon})_x + i(\boldsymbol{k} \times \boldsymbol{\varepsilon})_y]C^{F_2m_2}_{F_1m_1}\delta_{m_1m_{2\pm1}} + (\boldsymbol{k} \times \boldsymbol{\varepsilon})_z C^{F_2m_2}_{F_1m_1}\delta_{m_1m_2} \end{aligned} \tag{2.24}$$

2.7 *Electric dipole parity violating transition,* $E1_{pv}$

The $E1_{pnc}$ amplitude arises from the mixing of states of opposite parity. The mixing of p-character into the s-wavefunctions can be calculated perturbatively as

$$\overline{|ns\rangle} = |ns\rangle + \sum_{\alpha} \frac{|\alpha p\rangle\langle\alpha p|H_{pv}|ns\rangle}{E_{ns} - E_{\alpha p}}, \tag{2.25}$$

where $\overline{|ns\rangle}$ is the perturbed wavefunction, and the sum goes over all intermediate p states. Then, the electric dipole parity violating amplitude will be given by,

$$\begin{aligned} E1_{pv} &= \langle\overline{n's}| - e\boldsymbol{\varepsilon}\cdot\boldsymbol{r}|\overline{ns}\rangle \cong \langle\overline{n's}| - e\boldsymbol{\varepsilon}\cdot\boldsymbol{r}|\overline{ns}\rangle + \langle\overline{n's}| - e\boldsymbol{\varepsilon}\cdot\boldsymbol{r}|\overline{ns}\rangle \\ &= \sum_{\alpha}\left(\frac{\langle n's|H_{pv}^{\dagger}|\alpha p\rangle\langle\alpha p| - e\boldsymbol{\epsilon}\cdot\boldsymbol{r}|ns\rangle}{E_{n's} - E_{\alpha p}} + \frac{\langle n's| - e\boldsymbol{\epsilon}\cdot\boldsymbol{r}|\alpha p\rangle\langle\alpha p|H_{pv}|ns\rangle}{E_{ns} - E_{\alpha p}}\right) \end{aligned} \tag{2.26}$$

with $\boldsymbol{\varepsilon}$ being the oscillating electric field. Bouchiat explains in [9] and [19] the representation of equation 2.26 in the following format:

$$(E1_{F_1m_1}^{F_2m_2})_{pv} = iImE1_{pv}\langle F_2m_2|\boldsymbol{\varepsilon}\cdot\boldsymbol{\sigma}|F_1m_1\rangle \tag{2.27}$$

The matrix element we see here is exactly the same as the previous calculations. Therefore the E1 transition amplitude will be given by,

$$(E1_{F_1m_1}^{F_2m_2})_{pv} = iImE1_{pv}[(\pm\varepsilon_x + i\varepsilon_y)\delta_{m_1m_{2\pm1}} + \varepsilon_z\delta_{m_1m_2}]C_{F_1m_1}^{F_2m_2} \tag{2.28}$$

As it was said before, the weak interaction mixes some $p_{1/2}$ character into the $s_{1/2}$ state, and this can be illustrated in the following way [17]: The non-relativistic s wave function is given by $\psi_0 = \frac{1}{\sqrt{4\pi}}R_0(r)\chi$. Where R_0 is the radial wave function of the s-state, and χ is the two-component spinor (electron spin state). For the p wave function we have $\psi_1 = \frac{1}{\sqrt{4\pi}}R_1(r)(-\boldsymbol{\sigma}\boldsymbol{n})\chi$ where $\boldsymbol{n} = \frac{\boldsymbol{r}}{r}$ is the unit radius-vector. The resulting mixed wave function will be,

$$\psi = \frac{1}{\sqrt{4\pi}}[R_0(r) - i\eta R_1(r)\boldsymbol{\sigma}\boldsymbol{n}]\chi \tag{2.29}$$

Here, $i\eta$ is the mixing coefficient, and it is imaginary due to the time reversal invariance.The last expression can be rewritten in the following way,

$$\psi = \tfrac{1}{\sqrt{4\pi}} R_0(r) \left(1 - \tfrac{i}{2}\boldsymbol{\vartheta}\boldsymbol{n}\right) \chi.$$

Now it is possible to see that the mixture of states can be understood as a rotation of χ by an angle ϑ around the direction $\boldsymbol{n}$.

2.8 Transition Rate

Let's call W_{fi} the stimulated-transition probability from a state $|i\rangle$ to a state $|f\rangle$. If we have a delta-like resonance then,

$$W_{fi} = \frac{4\pi^2 e^2}{\hbar^2 c} \int dw' I^{w'} |\langle f|\boldsymbol{r}|i\rangle \delta(w_{fi} - w') \tag{2.30}$$

Where $\boldsymbol{D}_{fi} = \langle f|e\boldsymbol{r}|i\rangle$ is the dipole matrix element. And, $I^{w'} = I\delta(w - w')$. I is the total, and $I^{w'}$ the spectral, intensity of the laser. Since the spectral intensity is given by a delta function it is assumed that it is much more narrow than the transition. Considering a transition with finite width then the line shape function is a Lorentzian centered at frequency w,

$$\delta(w_{fi} - w') \to \frac{\gamma_t/\pi}{(w_{fi} - w')^2 + \gamma_t^2} \tag{2.31}$$

Where $\gamma_t = \frac{\gamma}{2}$ is the half-width of the transition. Then we will have,

$$\begin{aligned} W_{fi} &= \frac{4\pi^2 e^2}{\hbar^2 c} \int dw' I\delta(w - w') |\langle f|\boldsymbol{r}|i\rangle|^2 \frac{\gamma_t/\pi}{(w_{fi} - w')^2 + \gamma_t^2} \\ &= \frac{4\pi e^2}{\hbar^2 c} I |\langle f|\boldsymbol{r}|i\rangle|^2 \int dw' \delta(w - w') \frac{\gamma_t}{(w_{fi} - w')^2 + \gamma_t^2} \\ &= \frac{4\pi e^2}{\hbar^2 c} I |\langle f|\boldsymbol{r}|i\rangle|^2 \frac{\gamma_t(w)}{(w_{fi} - w)^2 + \gamma_t^2(w)} \\ &= \left(\frac{4\pi e^2}{\hbar^2 c} I \frac{|\langle f|\boldsymbol{r}|i\rangle|^2}{\gamma_t(w)}\right) \frac{\gamma_t^2(w)}{(w_{fi} - w)^2 + \gamma_t^2(w)} \end{aligned} \tag{2.32}$$

The Lorentzian term goes to 1 when the laser is on resonance, $w_{fi} = w$.

Then the transition rate for stimulated emission in CGS is given by:

$$W_{fi} = \frac{4\pi e^2}{\hbar^2 c} I \frac{|\langle f|\boldsymbol{r}|i\rangle|^2}{\gamma_t(w)} \tag{2.33}$$

According to [20],

$$W_{fi} = \frac{4\pi^2}{\hbar^2 c}\left(\frac{1}{4\pi\varepsilon_0}\right) I(w_{fi})|\boldsymbol{\varepsilon}\cdot\boldsymbol{D}_{fi}|^2 \tag{2.34}$$

Electric dipole moment matrix: $\boldsymbol{D}_{fi} = -e\boldsymbol{r}_{fi}$

$$W_{fi} = \frac{4\pi^2}{\hbar^2 c}\left(\frac{1}{4\pi\varepsilon_0}\right) I(w_{fi})|\boldsymbol{\varepsilon}\cdot(-e\boldsymbol{r}_{fi})|^2 \tag{2.35}$$

And we have,

$$W_{fi} = \frac{4\pi^2 e^2}{\hbar^2 c}\left(\frac{1}{4\pi\varepsilon_0}\right) I(w_{fi})|\boldsymbol{\varepsilon}\cdot\boldsymbol{r}_{fi}|^2 \tag{2.36}$$

Comparing equation 2.33 and equation 2.36:

$$W_{fi}^{CGS} = \frac{4\pi e^2 I}{\hbar^2 c}\frac{|\langle f|\boldsymbol{r}|i\rangle|^2}{\gamma_t(w)} = \frac{4\pi e^2 I}{\hbar^2 c}\frac{|\langle f|\boldsymbol{r}|i\rangle|^2}{\gamma(w)/2} = \frac{4\pi^2 e^2 I}{\hbar^2 c}\frac{2I}{\pi\gamma(w)}|\langle f|\boldsymbol{r}|i\rangle|^2 \tag{2.37}$$

And,

$$W_{fi} = \frac{4\pi e^2}{\hbar^2 c}\underbrace{\left(\frac{1}{4\pi\varepsilon_0}\right)}_{=1 in CGS} I(w_{fi})|\boldsymbol{\varepsilon}\cdot\boldsymbol{r}_{fi}|^2 = \frac{4\pi e^2}{\hbar^2 c} I(w_{fi})|\boldsymbol{\varepsilon}\cdot\boldsymbol{r}_{fi}|^2 \tag{2.38}$$

$$\begin{aligned}
\frac{4\pi^2 e^2 I}{\hbar^2 c}\frac{2I}{\pi\gamma(w)}|\langle f|\boldsymbol{r}|i\rangle|^2 &= \frac{4\pi e^2}{\hbar^2 c} I(w_{fi})|\boldsymbol{\varepsilon}\cdot\boldsymbol{r}_{fi}|^2 \\
\frac{2I}{\pi\gamma(w)}|\langle f|\boldsymbol{r}|i\rangle|^2 &= I(w_{fi})|\boldsymbol{\varepsilon}\cdot\boldsymbol{r}_{fi}|^2 \\
I(w_{fi}) &= \frac{2I}{\pi\gamma(w)}
\end{aligned} \tag{2.39}$$

Substituting the last equation into equation 2.36:

$$W_{fi} = \frac{4\pi^2 e^2}{\hbar^2 c}\left(\frac{1}{4\pi\varepsilon_0}\right) I(w_{fi})|\boldsymbol{\varepsilon}\cdot\boldsymbol{r}_{fi}|^2$$

Knowing that $\gamma = 1/\tau$, we have the transition rate for stimulated emission in SI is given by,

$$W_{fi} = \frac{2e^2}{\hbar^2 c\varepsilon_0} I|\boldsymbol{\varepsilon}\cdot\boldsymbol{r}_{fi}|^2\tau \tag{2.40}$$

Converting this last equation to au we will use the following substitutions: $e = 1$, $\hbar = 1$, $c = 137.035$, $c\varepsilon_0 = 10.904$. The relation between laser intensity and electric field strength is $I = E_0^2/2\eta$ where $\eta = 377\Omega$ in vacuum. Then,

$$W_{fi} = \frac{2e^2}{\hbar^2 c\varepsilon_o}\frac{E_0^2}{2\eta}|\boldsymbol{\varepsilon}\cdot\boldsymbol{r}_{fi}|^2\tau = |E_0\boldsymbol{\varepsilon}\cdot\boldsymbol{r}_{fi}|^2\tau \tag{2.41}$$

Then the transition rate for stimulated emission in atomic units is given by:

$$W_{fi} = |\boldsymbol{E}\cdot\boldsymbol{r}_{fi}|^2\tau \tag{2.42}$$

2.9 The hyperfine structure of Rb and Fr

Rubidium and Francium are alkalis which have a bound core and a single valence electron in its outermost shell.

Rubidium has two natural isotopes ^{85}Rb (72.2%) and ^{87}Rb (27.8%) with nuclear spins $I = \frac{5}{2}$ and $I = \frac{3}{2}$, respectively. Looking into the diagram of ^{85}Rb, for example, one can see that the ground state have hyperfine structure split apart by about 3GHz, then facilitating the adjustment of the laser to the desired transition.

According to the selection rules the only transitions allowed are between levels with $\Delta F = 0, \pm 1$.

2.10 The Zeeman spectrum

In order to excite a specific transition from one hyperfine state to another we apply a small static magnetic field that will split the spectral lines, and consequently slightly change their energies by a different amount. The m sublevels then will be in its reverse order according to figure 2.1:

This difference in energy is due to the Zeeman Hamiltonian given by,

$$H_Z = g_I\frac{\mu_N}{\hbar}\boldsymbol{I}\cdot\boldsymbol{B} \tag{2.43}$$

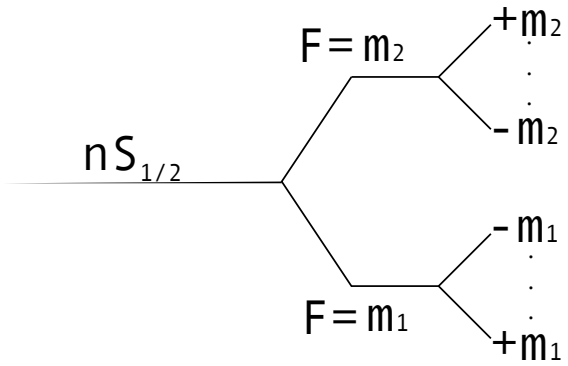

Figure 2.1: Generic diagram of the energy levels from the atomic ground state showing the Zeeman structure.

$\mu_N = e\hbar/2m_p$ is the nuclear magneton, $\boldsymbol{B}$ is the static magnetic field, and $\boldsymbol{I}$ is the nuclear spin. This gives us,

$$W_{Zeeman} = H_L + H_S + H_Z = \left(\frac{\mu_B}{\hbar}(\boldsymbol{L} + g_S\boldsymbol{S}) + g_I\frac{\mu_N}{\hbar}\boldsymbol{I}\right)\cdot\boldsymbol{B}, \tag{2.44}$$

where $\mu_B \sim 9\times10^{-24}JT^{-1}$ and $\mu_N \sim 5\times10^{-27}JT^{-1}$, and since $\mu_B \gg \mu_N$, the nuclear magneton is neglected. Lets consider the magnetic field being in the z-direction. For s-states L=0 and knowing that $S = \sigma/2$ and g_S is approximated to 2, the equation resumes to,

$$W_{Zeeman} = \frac{\mu_B}{\hbar}\boldsymbol{\sigma B} \tag{2.45}$$

Each m level will have a shift in frequency given by,

$$\Delta\nu_m = \frac{\mu_B}{\hbar}\langle nsFm|\sigma\cdot\boldsymbol{B}|nsFm\rangle = \mu_B g_F mB \tag{2.46}$$

According to the vector model for weak fields [21]:

$$g_F = g_J\frac{F(F+1)+J(J+1)-I(I+1)}{2F(F+1)} \tag{2.47}$$

g_J is 2 for s-states.

2.10.1 $\Delta F = 0$

According to [21] the splitting of spectral lines by the Zeeman effect between the two levels F_1 and F_2 will have their variation in frequencies defined as,

For $\Delta m = 0$:

$$\Delta\nu = (g_{F_2} - g_{F_1})m\mu_B B \tag{2.48}$$

For $\Delta m = \pm 1$:

$$\Delta\nu = [(g_{F_2} - g_{F_1})m_2 \pm g_{F_1}]\mu_B B \tag{2.49}$$

$\Delta\nu = \nu - \nu_0$ and ν_0 is zero in the absence of magnetic field. The total transition rate between two states will be proportional to the sum of all transition amplitudes involved, therefore we will have contribution from the parity conserving amplitudes, M1 and $E1_{Stark}$, and the parity violating amplitude, $E1_{pv}$. So we have:

For $q = \Delta m = 0$, $\sigma_{1,q} = \sigma_{1,0} = \sigma_z$, then,

$$\left(R_F^F\right)_{\Delta m=0} = \sum_m |\alpha \boldsymbol{E}\cdot\boldsymbol{\varepsilon} + C_{Fm}^{Fm}[i\beta(\boldsymbol{E}\times\boldsymbol{\varepsilon})_z + M1(\boldsymbol{k}\times\boldsymbol{\varepsilon})_z + iImE1_{pv}\varepsilon_z]|^2 \tag{2.50}$$

For $q = \Delta m = \pm 1$, $\sigma_{1,q} = \sigma_{1,\pm 1}$, then,

$$\begin{aligned}\left(R_F^F\right)_{\Delta m=\mp 1} = \sum_m |C_{Fm\pm 1}^{Fm}\{&\beta[(\boldsymbol{E}\times\boldsymbol{\varepsilon})_y \pm i(\boldsymbol{E}\times\boldsymbol{\varepsilon})_x] \\ &+ M1[(\boldsymbol{k}\times\boldsymbol{\varepsilon})_x + i(\boldsymbol{k}\times\boldsymbol{\varepsilon})_y] \pm iImE1_{pv}\varepsilon_z\}|^2\end{aligned} \tag{2.51}$$

This gives us 3 lines in the rate diagram, one for the $\Delta m = 0$ transition, and two more for $\Delta m = \pm 1$ transitions.

2.10.2 $\Delta F = \pm 1$

Let's consider an atom with ground state levels F_1 and F_2, which are split into the magnetic sub-levels $-m_1 ... + m_1$ and $-m_2 ... + m_2$, respectively. The first excited state follows the same pattern, $F_1' = -m_1 ... + m_1$, the same for F_2'. Remembering that $m_2 > m_1$. For $\Delta m = 0$ there will be $2m_1 + 1$ possible transitions, being single

lines. For $\Delta m = \pm 1$ there will be $2m_2$ transitions, each one being constituted by 2 lines, one for $\Delta m = +1$, and the other for $\Delta m = -1$. These lines happen between the $\Delta m = 0$ hyperfine transitions. The equations for transition rates between these states are:

For $\Delta m = 0$:

$$\left(R_{Fm'}^{F'm'}\right) = \left(C_{Fm'}^{F'm'}\right)^2 |i\beta(\boldsymbol{E} \times \boldsymbol{\varepsilon})_z + M1(\boldsymbol{k} \times \boldsymbol{\varepsilon})_z + iImE1_{pv}\varepsilon_z]|^2 \tag{2.52}$$

For $\Delta m = \pm 1$:

$$\left(R_F^{F'}\right)_q = R_{F,q-1}^{F',q} + R_{F,q}^{F',q-1} \tag{2.53}$$

with,

$$\begin{aligned} R_{F,q\pm1}^{F',q} = & \left(C_{F,q\pm1}^{F',q}\right)^2 |\beta[(\boldsymbol{E} \times \boldsymbol{\varepsilon})_y \pm i(\boldsymbol{E} \times \boldsymbol{\varepsilon})_x] \\ & + M1[(\boldsymbol{k} \times \boldsymbol{\varepsilon})_x + i(\boldsymbol{k} \times \boldsymbol{\varepsilon})_y] \pm iImE1_{pv}\varepsilon_z|^2. \end{aligned} \tag{2.54}$$

Chapter 3

TRAPPING AND COOLING OF NEUTRAL ATOMS

3.1 Motivation for the use of a trap

The experiment performed until 1998 at the University of Colorado by the Boulder group, that measured the amplitude of the parity forbidden transition between the $6s \rightarrow 7s$ states of cesium, increased the accuracy for the nuclear spin independent amplitude to 0.35%, and represents the culmination of atomic parity violation measurements to date.

Roughly speaking, the experiment measured a tiny ($\approx 10^{-5}$) change in excitation probability under parity reversals (i.e. reversals of externally applied electric and magnetic fields, laser polarization, and switches between $|6sFm\rangle$ and $|6sF-m\rangle$ states) on an already very weak Stark-induced $6s - 7s$ transition. In comparison to most experiments in atomic physics, the excitation rate per atom is very small in this type of experiment, and to obtain a sizeable overall signal, a large number of atoms have to be probed. In the Boulder experiment it was possible to have 10^{13} to $10^{15} s^{-1} cm^{-2}$ atoms in the beam. However, this will not be possible for francium and other radioactive isotopes, neither now nor in the foreseeable future. At the ISOLDE radioactive beam facility at CERN in Geneva, Switzerland, peak production of $\approx 10^{10}$ s^{-1} for the best Fr isotopes has been achieved, and the upcoming actinide targets at ISAC at TRIUMF in Vancouver hopefully will reach similar production levels. Figure 3.1 shows some achieved and estimated production yields for Fr isotopes.

Atomic parity violation experiments with short-lived radioactive isotopes hence appear presently not feasible. However, it must be noted that a thermal atomic beam

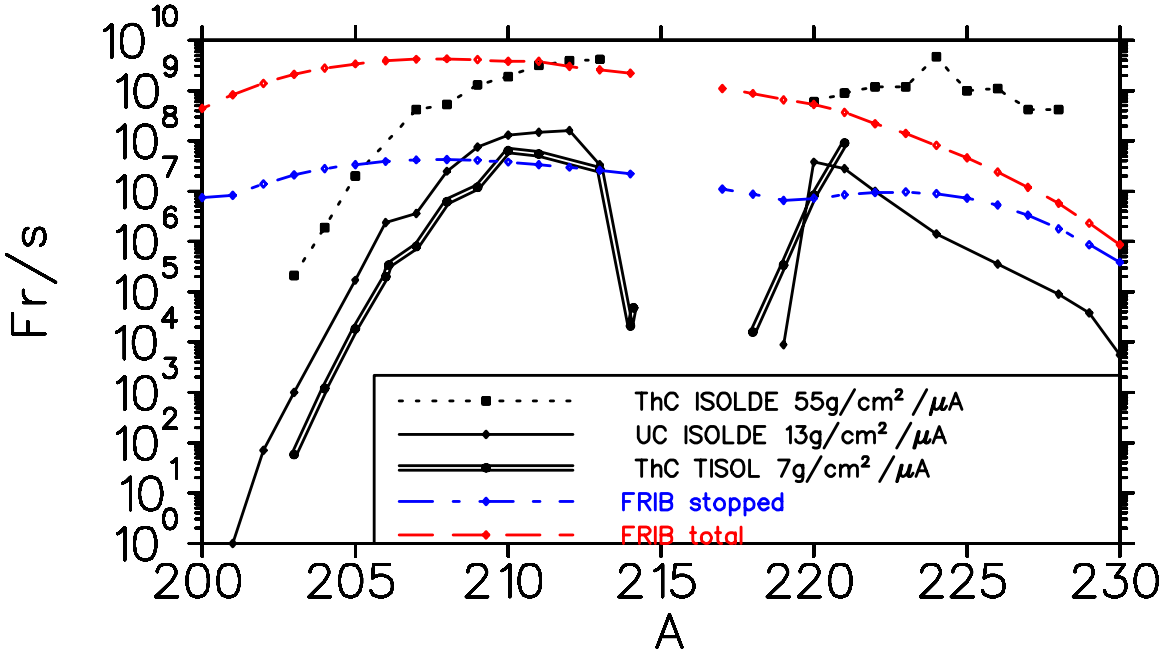

Figure 3.1: Francium production yields at ISOLDE; FRIB refers to the upcoming radioactive beam facility at Michigan State University; courtesy John Behr, TRIUMF.

makes very inefficient use of the atoms.

In an atomic beam, the atoms traverse the crossed laser beam in a few microseconds and are then lost forever. On the other hand, with the cooling and trapping techniques, it is possible to expose a single atom, from seconds to minutes, to the laser light. The atomic beam has high speed and is subject to Doppler broadening due to its divergence, tuning a fraction of the atoms in the beam out of resonance with the laser. In a magneto-optical trap (MOT) one can neglect the effects of Doppler broadening, thus all atoms being used in the experiment can contribute.

Relatively soon after the methods of cooling and trapping with laser light were pioneered in the 1980s, the use of a laser trap with small samples of radioactive isotopes was discussed, and groups at Stony Brook, Berkeley, and Boulder started to work on on-line trapping setups for beta-decay and atomic parity violation experiments [28, 29, 30].

In this type of measurement, the signal rate is proportional to the density of atoms in the interaction region. The amount of atoms used in an experiment with atomic beams or vapor cells is much higher than in an experiment where the atoms will be cooled then trapped, but the atomic density between both techniques is equivalent, making the later an efficient alternative in cases where the quantity of atoms available are not sufficient.

The benchmark is the number of $6s \rightarrow 7s$ excitations per second reported by Wood et al. for their final Cs APNC experiment, which is $\approx 10^{10}$ [25]. To avoid photoionization of excited Fr atoms in the $8s$ and $7p_{3/2}$ states, which would remove the atoms permanently from the trap, we estimate a maximum, 'safe' $7s \rightarrow 8s$ excitation rate of 30 Hz (see below), suggesting that 3×10^8 trapped atoms could provide a similar signal, if the parity violating asymmetry in the signal was identical. However, $E1_{\mathrm{PNC}}$is 18× larger in Fr than in Cs[26, 27], leading for comparable Stark amplitudes to an 18× larger asymmetry, which enters squared into the the expression for the signal-to-noise ratio. Considering these factors, and taking into account the fact that the MOT is at most available for the measurement for half of the time (trapping and cooling atoms during the rest of the time), we find that approximately 2×10^6 Fr atoms in the interaction region would deliver a signal of comparable quality as the 1998 Boulder experiment (and a trap with 2.8×10^5 Fr atoms for the 1988 Boulder apparatus). Based on the number of trapped Fr atoms achieved at Stony Brook and the projected flux to be delivered at TRIUMF, this should be achievable.

This discussion shows that for radioactive isotopes, the use of laser trapping (or cooling, see discussion in [sanguinetti]) is indispensable, motivating the laser trap project described in this thesis. In the following, we give an introduction to the MOT, which plays the central role in the setup.

3.2 Doppler Cooling

In order to understand the process of laser cooling neutral atoms let's suppose a two-level atom as shown in figure 3.2.

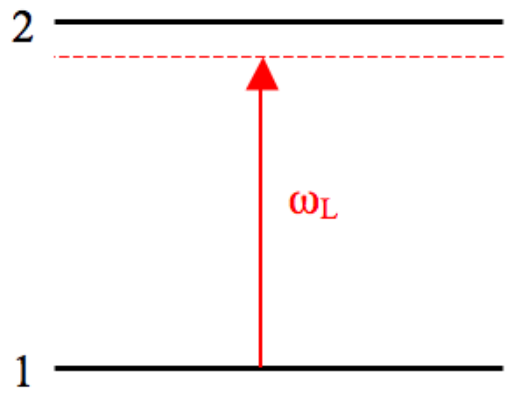

Figure 3.2: A two-level atom. The laser frequency is red-shifted by a few linewidths.

The laser frequency ω_L is slightly detuned (decreased) from resonance, such that $\Delta\omega = \omega_L - \omega_{12} \approx -\Gamma$, where ω_{12} is the frequency of the atomic transition, and Γ the natural linewidth of the excited state. Light of opposite circular polarization is sent through both sides of an atomic vapor cell.

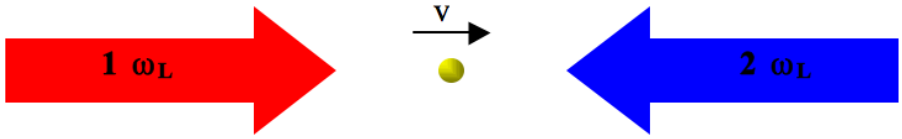

Figure 3.3: Principle of Doppler cooling. Figure in the atom frame.

In the laboratory frame, both beams will be at the same frequency ω_L. From the point of view of the moving atoms inside of the cell the beams are at different frequencies due to the Doppler effect: the beam the atom is traveling towards (beam

2) will be blue shifted, while the beam that goes in the same direction the atom's motion (beam 1) is red shifted (figure 3.3). The laser frequencies in the atom's frame are given by $\omega_{beam1} = \omega_L(1-\frac{v}{c})$ and $\omega_{beam2} = \omega_L(1+\frac{v}{c})$, where v is the atom's velocity. The atoms will absorb more photons from the beam whose frequency is up shifted due to the Doppler effect, re-emitting them right after without preferred direction. The closer the laser energy is from resonance, the faster the absorption and re-emission of photons will happen.

The scattering of photons from the atoms will make them lose momentum equivalent to the momentum of the photon absorbed, $\hbar\frac{\omega_L}{c}$, reducing its kinetic energy and then *laser cooling* the atoms with help of the Doppler effect.

What was explained above can be expanded to a three-dimensional configuration by using three counter-propagating pairs of beams, which will work as a viscous force on the atoms slowing them down until the Doppler cooling limit, given by

$$T_{Doppler} = \frac{\hbar\Gamma}{2k_B}, \tag{3.1}$$

where Γ is the width of the spectral line (natural linewidth), $\hbar$ the reduced Planck's constant, and k_B the Boltzmann's constant. This laser cooling technique is called *optical molasses*.

The atoms contained in the vapor cell which were cooled down have a lifetime dependent on their collisions with the hot (room temperature) background gas. The hot atoms have so much more energy that virtually all collisions lead to the loss of the cold atom from the molasses. To achieve a reasonable life time of the molasses, the background gas must be very dilute, around 10^{-8} mbar or less.

Optical molasses generates a *velocity dependent* force, as the name implies.

3.3 Trapping

The velocity-dependent force applied to the gas, inside of the glass cell, slowed down the atoms forming the optical molasses. But only this force does not guarantees that

the atoms will remain in the same place. If one waits long enough, they might start moving away from the central region where they were trapped by the laser beams.

In order for this not to happen, and to have a real trap, it is essential to add a position-dependent force to the system. This force will set spatial boundaries to the atoms not allowing them to escape from the center of the trap.

This is done by placing two conducting circular coils in an anti-Helmholtz mode around the region where the laser beams intersect. In the Helmholtz configuration the coils are separated by a distance that is equal to its radius, having the same amount of current flowing in the same direction, so that it generates a uniform magnetic field in the middle of the two magnetic coils. The anti-Helmholtz configuration has current flowing in opposite directions through the coils, giving rise to a magnetic field gradient that is zero right at the middle and increases its strength along with the distance from the mid-plane between the coils.

While light is being sent through opposite sides of the cell decreasing the velocity of the atoms, a magnetic field gradient is applied to the system. As can be seen in figure 3.4. The radial magnetic field applied will lift the degeneracies of the energy levels as the atoms moves away from the center. The magnetic field increases radially and its coupling to the atomic magnetic moment generates a restoring force that brings the neutral atoms back to the position of minimum energy state. This force has a position dependence on the Zeeman splitting of the electronic levels, which are split more and more as the atom moves away from the origin.

In the example of the two-level atom showed in figure 3.4 one can see the two beams of light of opposite circular polarization hitting the gas from both sides while the atoms move in the z direction. For simplicity, a transition $J = 0 \rightarrow J = 1$ is chosen.

The degeneracy of the excited state, $J = 1$, will be lifted by the magnetic field gradient applied, which gets stronger as it moves away from the center of the trap.

The slightly red-detuned laser beam will resonate on the right with the transition

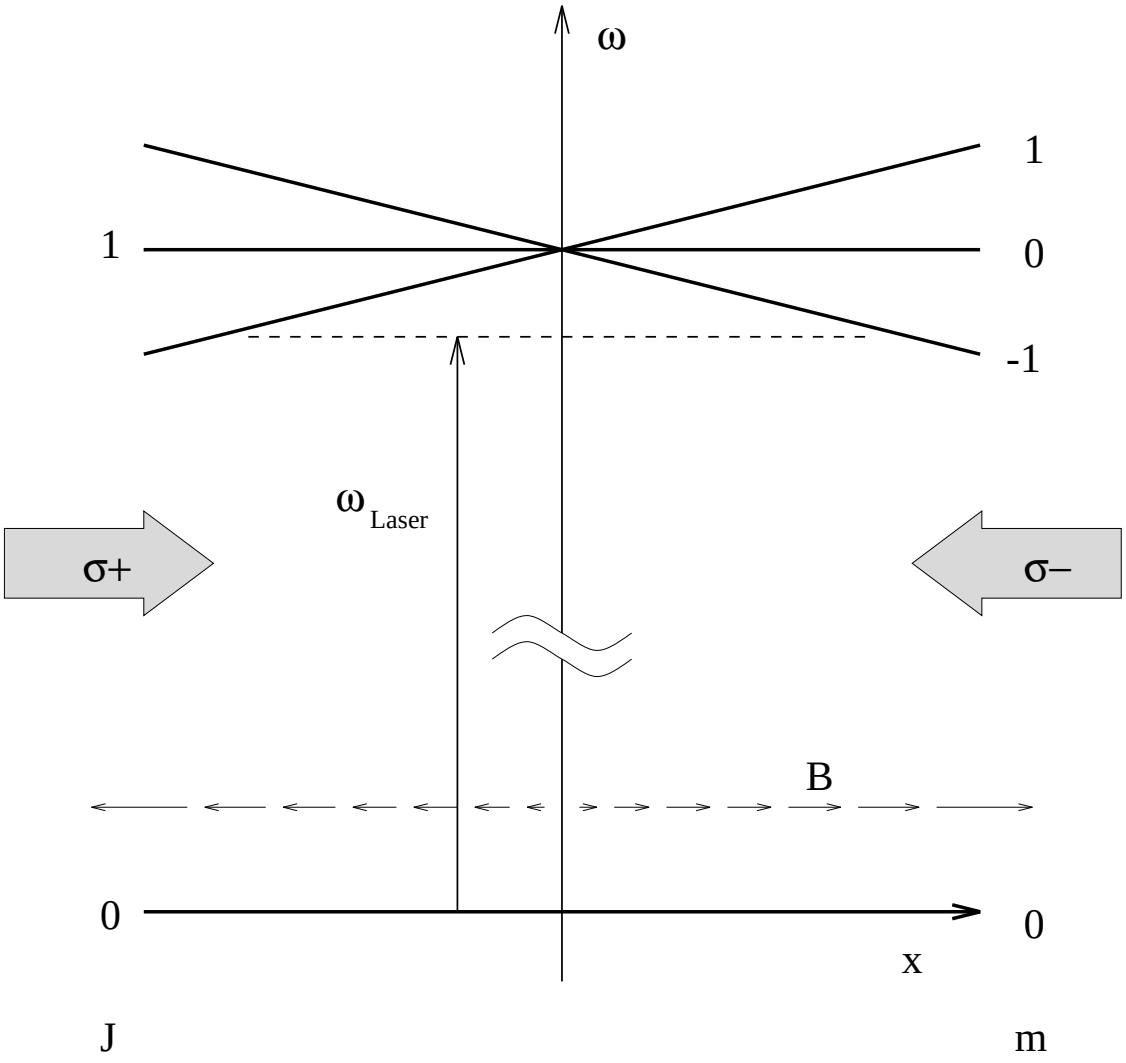

Figure 3.4: Magnetic field gradient and polarization: position dependence force [31].

$J = 0, m = 0 \rightarrow J = 0, m = -1$, and on the left with $J = 0, m = 0 \rightarrow J = 0, m = 1$. If we choose the polarizations of the laser beams such that the beam coming from the left is σ_+ and the one from the right σ_-, the atom will preferably absorb photons such that the momentum transfer pushes it towards the center.

Since the laser frequency is slightly detuned to the red by $\approx \Gamma$, a velocity dependent force is added due to the Doppler effect caused by the motions of the atoms. The restoring force acting on the atoms will be then given by the contribution of two linear terms, one dependent on the atomic displacement and the other on the atomic velocity.

$$\begin{aligned} F_{MOT} &= \frac{\Delta p}{\Delta t} \\ &= \frac{\hbar\kappa\Gamma}{2}\left(\frac{S_0}{1+S_0+\frac{4(\Delta\omega-\boldsymbol{\kappa}\cdot\boldsymbol{v}-\beta x)^2}{\Gamma^2}} - \frac{S_0}{1+S_0+\frac{4(\Delta\omega+\boldsymbol{\kappa}\cdot\boldsymbol{v}+\beta x)^2}{\Gamma^2}}\right) \end{aligned} \tag{3.2}$$

In equation 3.2, S_0 is the saturation parameter, which is given by the laser intensity divided by the transition saturation intensity. $\Delta\omega = \omega - \omega_0$ is the laser detuning, and βx represents the Zeeman effect for a spatially constant magnetic field gradient, where x is the coordinate with respect to the center, as can be seen in figure 3.4.

When $S_0 = 1$ the radiation pressure acting on an atom in resonance will be given simply by $F_{MOT} = \frac{\hbar\kappa\Gamma}{2}$.

In the case of weak saturation, i.e. $S_0 << 1$, when the atoms are around the centre of the trap and consequently are moving with low velocities and under a weak magnetic field, the denominator of equation 3.2 can be developed such that the final result predicts the atoms will behave as a damped harmonic oscillator.

3.4 The Real World Magneto-Optical Trap

In the real MOT things become more intricate, since now one has to think about the trap as a three-dimensional object (figure 3.5), and take into account the splitting of the hyperfine structure of the atomic energy levels.

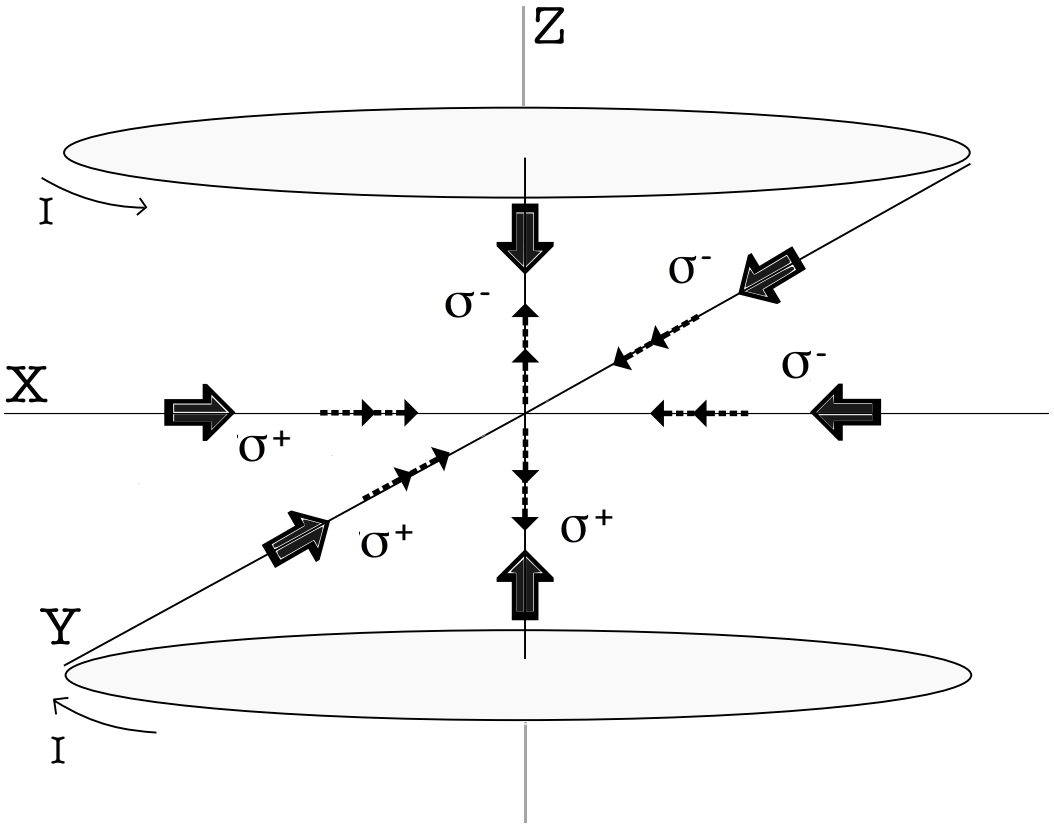

Figure 3.5: Scheme for the MOT in three dimensions.

The alkali atoms going to be trapped generally have a non-zero nuclear spin I. The simplest situation $J = 1/2 \rightarrow J = 3/2$, where one has the $ns_{1/2} \rightarrow p_{3/2}$ configuration, the ground state is split into two levels, and the first excited state into four, giving rise to a multilevel arrangement. Despite the complexity added, this circumstance does not prevent the MOT from working quite well. It is necessary to keep the system in a two-level configuration, but the presence of two ground state sub-levels can be a problem, as is illustrated in figure 3.6. In order for an atom to be trapped and cooled it must go through many cycles of absorption followed by spontaneous emission. Thus the atom needs to have what is generally referred to as a closed transition, such that

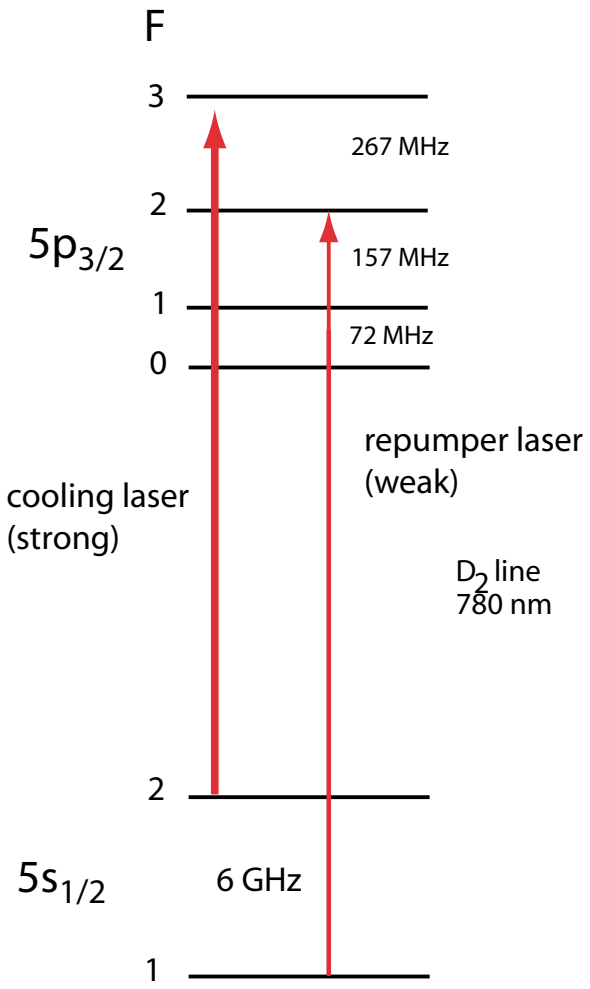

Figure 3.6: Principle of the repumper.

after each excitation it will decay back to the lower state is was originally in. ^{87}Rb has an almost-closed $5s_{1/2}F = 2 \rightarrow 5p_{3/2}F = 3$ transition (figure 3.6) .

In the electric dipole approximation the selection rules state that the change in angular momentum between the final and initial states must be $\Delta F = 0, \pm 1$. Therefore an atom excited to level $5p_{3/2}F = 3$ can only decay to $5s_{1/2}F = 2$.

The transition $5s_{1/2}F = 2 \rightarrow 5p_{3/2}F = 2$ might occur due to the linewidths of the states and of the laser. When this happen the atom excited to the a$5p_{3/2}F = 2$ is then allowed to decay to $5s_{1/2}F = 1$ 'dark' state. Once the atom falls in the dark

state the cycle between ground and excited state is interrupted, stopping the atom of being laser trapped and cooled. In order to keep the atom in a two-level scheme and the loop between absorption and spontaneous emission going, a 'repumper' laser beam resonant with the $5s_{1/2}F = 1 \rightarrow 5p_{3/2}F = 2$ transition will excite the atoms from the dark state, repopulating the $5s_{1/2}F = 2 \rightarrow 5p_{3/2}F = 3$ cycle.

3.4.1 Capture Efficiency: Zeeman Slower versus Vapor Cell MOT

An important factor to take into account when trapping atoms is that at room-temperature they are too fast to be captured by the MOT, resulting in a negligible amount of atoms in the trapping region. Therefore it is necessary to first slow them down to an approximate standstill condition.

There are two main techniques that can solve this problem, helping to enhance the capture efficiency of the system: Zeeman slower, and vapor cell MOT.

In the **Zeeman slower** the atomic beam coming from the oven overlaps with the counter-propagating laser beam which slow down the atoms by means of spontaneous emissions (figure 3.7). The slowing laser beam is adjusted to be resonant to the atomic transition, and to keep it like that, as the atoms loose velocity, a solenoid creates a varying magnetic field along the way, shifting the atomic resonance.

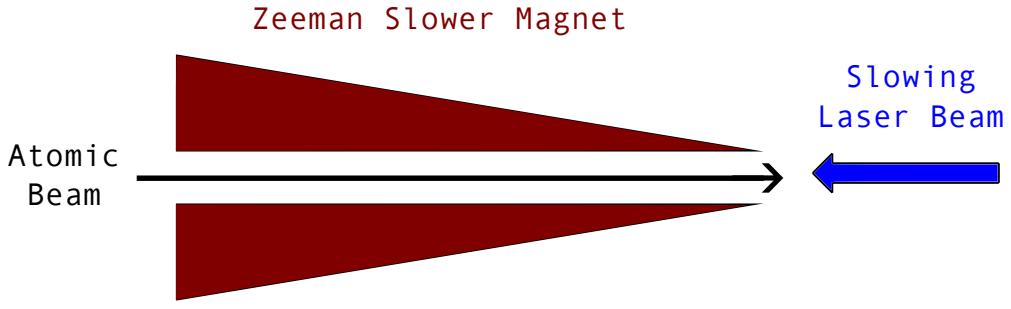

Figure 3.7: Zeeman slower.

The **vapor-cell MOT** configuration consist of having the MOT inside of a vapor cell, at ambient temperature and very low pressure, approximately $10^{-8}mbar$, which can be controlled to some extent by changing the temperature of the source; the heating or cooling of the source leads to higher or lower vapor pressure, respectively [32].

Once the atoms leave the oven, they have a wide range of velocities according to the Maxwell-Boltzmann distribution, and travel in random directions. To guarantee an effective cooling it is necessary to load the trap with slow atoms, since only the ones localized in the low-velocity tail of the distribution are captured by the MOT. Eventually the atoms will pass through the trap and might be cooled by the radiation pressure from the laser beams if they are below a maximum capture velocity, as can be seen in figure 3.8.

The net force acting against the movement of the atoms has a significant size only when

$$|\Delta\omega - \boldsymbol{k} \cdot \boldsymbol{v}| \leq \frac{\Gamma}{2}\sqrt{1 + S_0}, \tag{3.3}$$

decelerating just a narrow velocity group of atoms for a certain detuning $\Delta\omega$.

Thus the light beams from the MOT select the slower atoms and trap them apart from the vapor. The remaining atoms in the vapor will re-thermalize through wall collisions, forming a new Maxwell-Boltzmann distribution and consequently replenishing the tail, from which the trap keeps capturing.

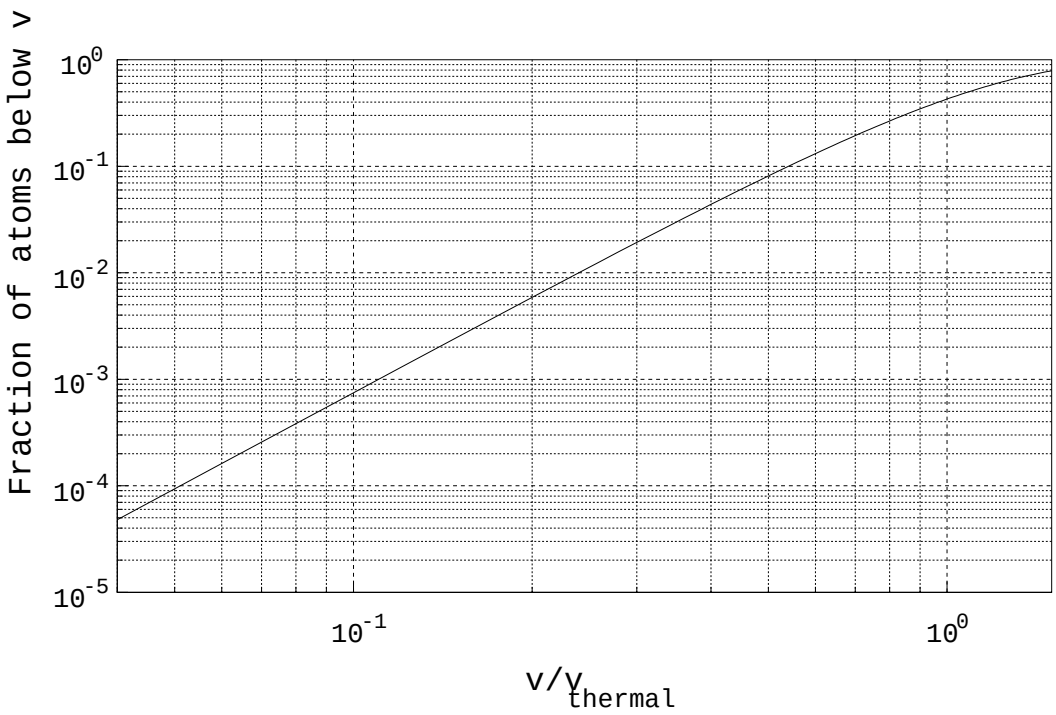

Figure 3.8: Fraction of capture atoms as a function of the maximum capture velocity v of the MOT. Two of the most powerful MOTS, C.Chu's Cs MOT and the author's Fr MOT, reach capture velocities of $v/v_w \approx 0.2$. Even these traps can only capture 1/200 of all atoms from a thermal beam. Source: G. Gwinner, ca. 1995.

Chapter 4

EXPERIMENTAL SETUP

4.1 Overview

In the previous chapter, the need for trapping and cooling of francium atoms was motivated. For work with rubidium at the University of Manitoba, the requirements are different, and in principle, an atomic beam could be used. However, a main motivation for the off-line work with a stable atom is to study and implement methods to be used later on with francium, and for this reason, a magneto-optical trap is used for Rb as well. In the following, we describe the Rb setup as it is currently being implemented at Manitoba.

The requirements posed on the laser system for atom-trapping work are substantial. The trapping laser needs to be single-mode, and typically should have at least 50mW of power. It is also necessary to frequency-stabilize its linewidth to around 1MHz or less, which is considerably smaller than the Doppler width.

For Rb (D_2 lines at 780 nm), commercially available tuneable diode laser systems can produce several hundred mW single mode, for US$10-20k. However, these diode lasers as delivered need significant additional work to be suitable for trapping. To have the correct conditions for operation one has to find a suitable mode and make the laser operate on that single mode. Once this is done the mode needs to be moved to the right frequency so that the Rb resonance can be found. Then it needs to be confirmed that the linewidth of the laser is still narrow. Finally, since the laser tends to drift in frequency with time (temperature and pressure fluctuations), it frequency has to be actively stabilized to the atomic resonance using an electronic feedback

mechanism.

To achieve the linewidth required for laser trapping (less than a few MHz), the diode laser chip has to operate inside an extended cavity. The length of this cavity has to be carefully controlled to maintain the correct frequency. To do all this, an optical setup is required that takes up more space and resources than the MOT itself. Figure 4.1 gives an overview of all components used. After briefly introducing the various components, their purpose and their interplay, the following sections will introduce the subsystems in detail.

The trap laser (Toptica DL100) produces about 150 mW of single-mode light at 780 nm. To avoid feedback into the laser by reflections within the setup, the light passes an optical diode based on Faraday rotation right after it exits the laser enclosure. The bulk of the light is sent to the MOT setup, but some amount of light is coupled into diagnostics required to stabilize the laser frequency. This is generally done using polarizing beam splitters (PBS). Before entering the PBS, the linearly polarized light passes a half-wave plate (HWP). By rotating of the HWP, the power on the two output ports of the PBS can be split up continuously in a wide range of ratios, allowing one to couple the required amount of light into the diagnostics sections.

Light from all lasers can be coupled into a Fabry-Perot cavity (Thorlabs S-200-7A, nominal range 780 nm - 930 nm, finesse 300) to test for single mode operation and laser bandwidth. When used with the TA-SHG laser at the fundamental (993 nm), the cavity still works, but with a quite low finesse.

When tuning up the system, the light can first be coupled into a high-precision wavemeter (Bristol 621) which displays the current laser frequency on a computer. The accuracy is sufficient to get the laser well within one GHz of the desired frequency. For more precise positioning of the laser relative to the Rb resonance, a small amount ($\approx$ 10 mW) of the laser light is diverted to a saturation spectroscopy setup. The light passes through a Rb vapor cell and resonant absorption of laser light

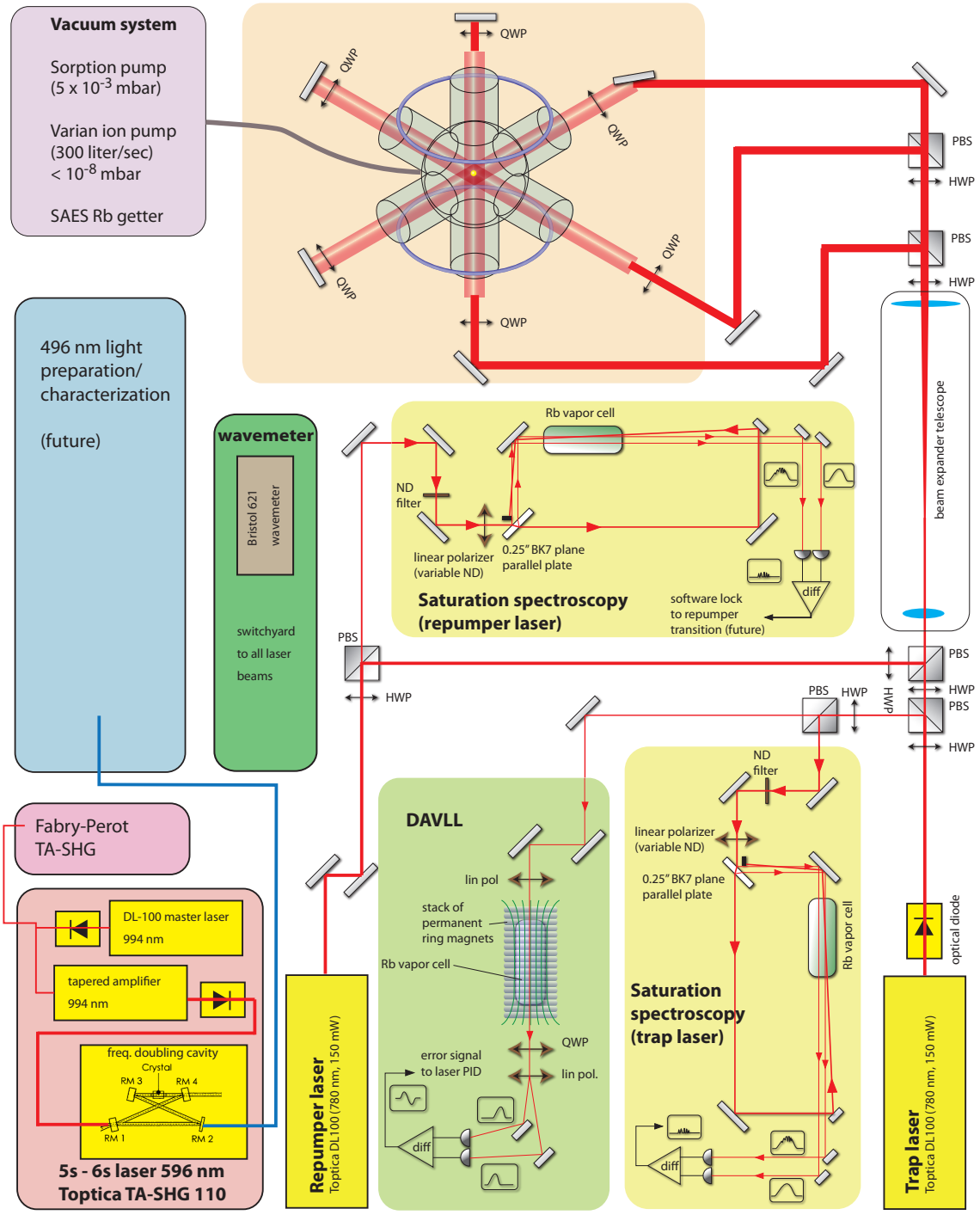

Figure 4.1: Layout of the experiment.

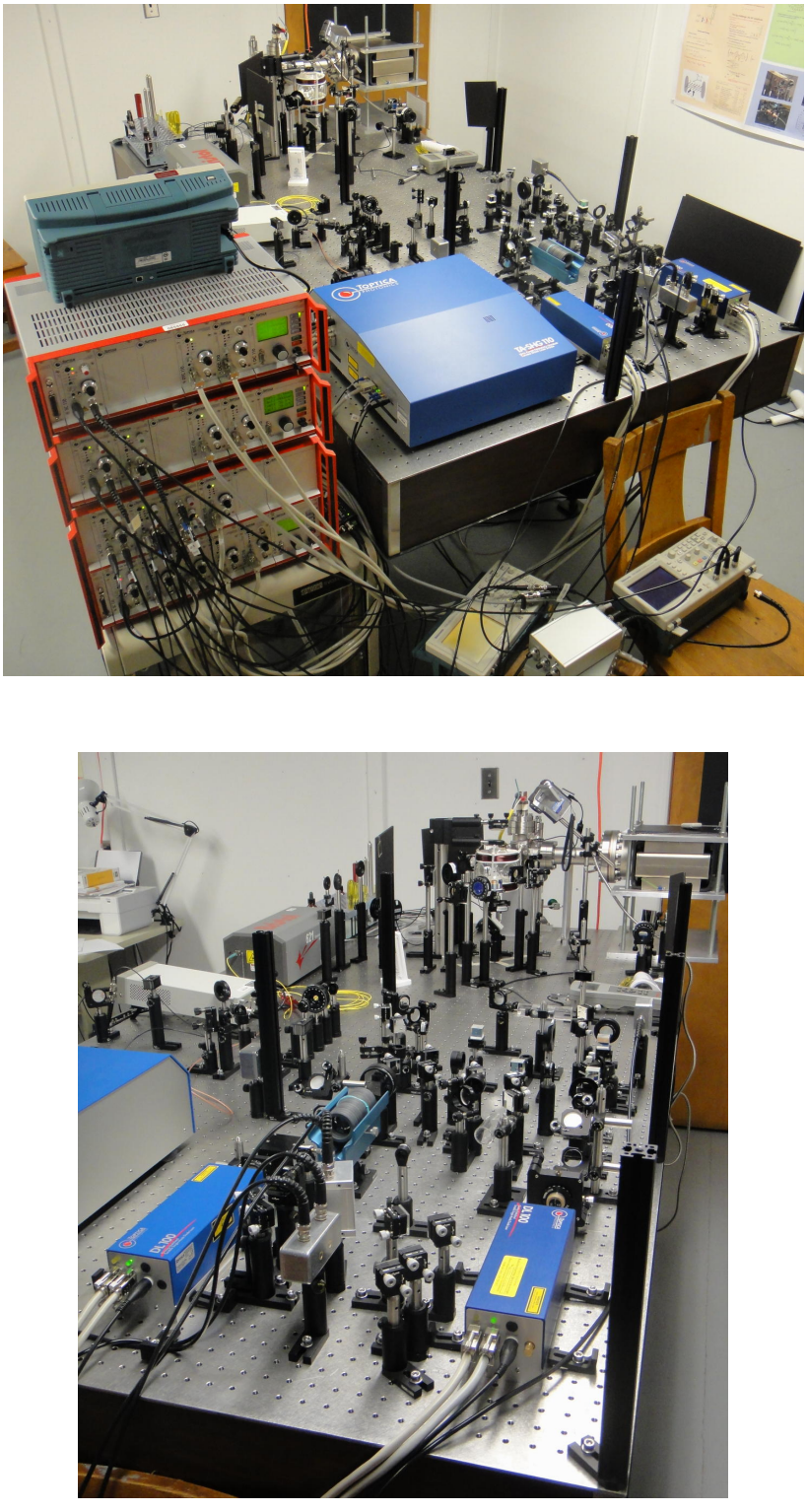

Figure 4.2: The optics table for the laser trap. Normally, the diagnostics setup and the DL100 lasers are inside a black foamboard box which has been removed for this picture.

indicates the presence of the Rb resonance. To increase the resolution of the absorption spectroscopy beyond the Doppler broadening of $\gtrsim 500$ MHz, we use a technique referred to as saturation spectroscopy, explained below in more detail. As a result, the excited-state hyperfine splitting is resolved, at a resolution close to the natural linewidth. The saturation spectroscopy setup allows to set the laser frequency to one of the atomic resonances with an accuracy at the MHz level. It also allows to judge the bandwidth of the laser radiation and confirm that the laser operates on a single mode.

Saturation spectroscopy is also often used to actively stabilize the laser to an atomic resonance, by 'locking' to a resonance peak. One complication of a MOT is that the trap laser must be kept a few linewidths to the red of the actual resonance. While this can be solved by shifting the light going to the MOT relative to the part entering the saturation spectroscopy using e.g. acousto-optic modulators, we chose to employ a simpler method deviced by the Wieman group, a dichroic atomic vapor laser lock (DAVLL) [33]. This scheme (also explained below in detail), allows us to shift the lock point for the laser continuously across a wide range within the Doppler-broadened absorption resonance. In conjunction with the DAVLL, saturation spectroscopy provide the absolute frequency information.

The repumper laser (Toptica DL100) is operated in a similar way. However, it can be locked directly to the resonance ($F = 1 \rightarrow F' = 2$ in ^{87} Rb and $F = 2 \rightarrow F' = 3$ in ^{85} Rb) without the need for an offset. Currently, the repumper is not locked, but is manually placed on the required resonance using saturation spectroscopy. In the future it will be locked to the resonance using a digital lock using software (LabView) on a PC.

After the diagnostics beams are taken off, the trap and repumper lasers are joined in a PBS into a single beam. A telescope expands the beam to around 15 mm diameter and delivers it to the MOT.

An additional laser on the table, a frequency-doubled diode laser system (Toptica

TA-SHG-100) provides up to 100 mW of light at 496 nm by frequency-doubling 993 nm radiation in a non-linear crystal.

4.2 Components of the laser trap setup

4.2.1 The Diode Laser System

Diode lasers are able to produce up to hundreds of mW of single-mode light, making them an ideal tool for atom trapping and laser spectroscopy, but their stabilization is a task that requires patience and caution to make sure external factors like changes in temperature or mechanical vibrations are not affecting its stability. A review of the basic properties of diode lasers and an introduction to their use in atomic physics is found in [34].

The current injected in the diode, which is localized inside of a resonance cavity, will promote the population inversion of the carriers from the laser medium, giving rise to stimulated emission that will generate the laser beam, which has longitudinal and transverse modes. Longitudinal modes result from the boundary conditions of the lasing cavity, which only allows modes that have an integer number of half-wavelengths, strengthening them by constructive interference and inhibiting the others by destructive interference. The modes generated inside of the cavity will compete but only the ones which dominate the optical gain will reach the lasing threshold. At the threshold stimulated emission dominates over spontaneous emission and the dominating mode has its intensity reinforced. Transverse modes refer to the spatial variation in a plane that is perpendicular to the light's propagation direction due to changes in current and refractive index of the material used to build the diode laser. Diode lasers can work in a single transverse (Gaussian) mode, so the beam cross-section has stronger intensity in the middle and lower in its outside limits. Such a beam profile is generally preferred. A deterioration in the profile is usually an indication of irreversible damage to the laser diode, which then requires replacement.

As the injection current is increased, the diode reaches the threshold of laser activity, and above this point the laser power increases roughly linearly with the injection current. Both the temperature and the injection current influence the frequency of the laser. On one hand, this provides the desired frequency tunability, but on the other hand, they must be carefully controlled to maintain frequency stability. The variations in temperature affect the gain, the optical length through thermal expansion of the lasing cavity, and the refractive index. Changes in the injection current also affect the refractive index of the the cavity due to the number of charge carriers, and also modify the temperature through resistive heating.

When tuning a diode laser using current and temperature, one has to be aware of mode hops. As said before, the change in temperature alters the cavity length, therefore the resonator that was operating on a single mode suddenly jumps to another mode or sometimes to multimodes, suddenly shifting the wavelength. Sometimes, a specific wavelength well within the tuning range might not be accessible at all as the diode simply mode-hops back and forth. An external cavity as used in our system (see below) largely alleviates this problem.

A scheme of the Toptica DL 100 diode laser head can be seen in figure 4.3. The Peltier element localized between a solid base block (heat reservoir) and the laser base plate is responsible for adjusting the temperature by transferring heat from one of its sides to the other. Both bases are connected by plastic screws for means of insulation. The temperature reading is made with a sensor localized in the laser base plate, which sends an error signal to the peltier element in order to keep the temperature of the diode actively stabilized. In order to tune the laser to the right frequency one has to precisely adjust temperature and injection current, and then look for fluorescence inside of a cell filled with rubidium vapor.

Free running diode lasers in general are not completely ready for operation due to instabilities and the possibility of having a large single mode width, not providing the necessary conditions for the use in a MOT. The technique of using an external

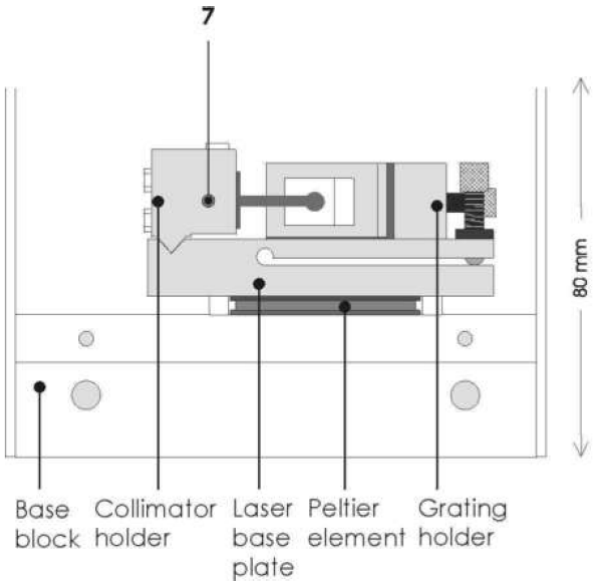

Figure 4.3: Schematic Drawing of the Diode Laser Head DL 100. Figure extracted from Toptica Photonics Manual.

cavity with optical feedback is then used in order to narrow the width of the single longitudinal mode. In many diode laser systems, the external cavity is formed by one of the end facets of the diode and a diffraction grating (for our system in the so-called Littrow configuration) at the other. Adjustment of the external cavity provides an additional way to scan the frequency of the laser, it improves the mode-hop free tunability range, and it also narrows the single-mode linewidth. The Quality factor, or simply Q factor, of the resonator indicates how much energy is being lost with respect to the amount of energy stored inside of the laser cavity. A high Q factor is an indication of low energy loss which, with the presence of an external cavity, may be achieved because the cavity increases the time-of-flight of the photons inside of the gain medium, rising the number of stimulated emissions, and consequently suppressing the amount of spontaneous emissions. Thus the spectral bandwidth becomes narrower. Without an external cavity laser diodes have linewidths of approximately

100 MHz, whereas an external cavity can narrow down the linewidth to 1 MHz or less.

In the DL 100 model, a diffraction grating in the Littrow configuration is the mechanism that regulates the feedback into the lasing medium in order to select the modes. In this configuration (see figure 4.4), $\theta_m = \theta_i$, i.e., the first-order beam is diffracted in the same direction as the incident beam, while the zeroth-order is reflected off the grating as an output beam.

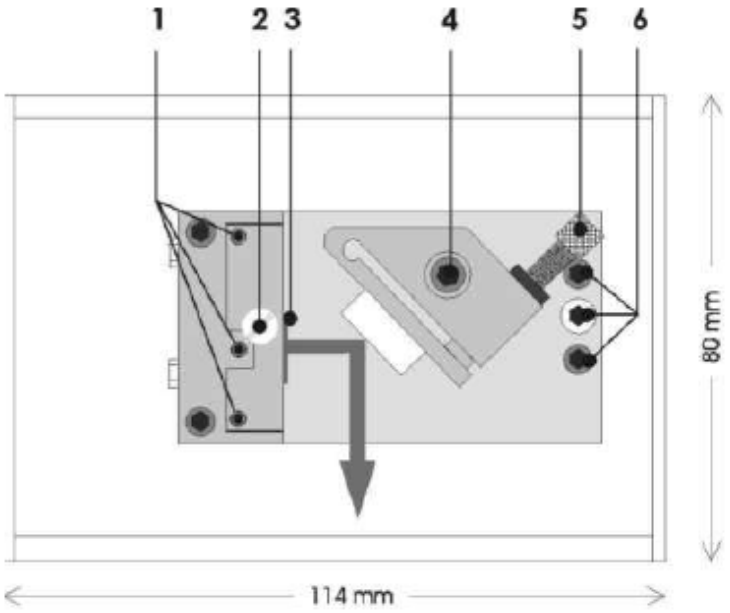

Figure 4.4: Littrow setup. Figure extracted from Toptica Photonics Manual.

The grating equation is given by,

$$m\lambda = d(sin\theta_m + sin\theta_i). \tag{4.1}$$

Since the mth-order diffracted beam angle, θ_m, coincides with the incident beam angle, θ_i, the grating equation becomes

$$m\lambda = 2dsin\theta, \tag{4.2}$$

where θ is the Littrow angle, between the normal with respect to the grating and the incident beam, for a grating of groove spacing d, and a given wavelength λ. The first-order diffracted beam will provide feedback to the laser diode.

By adjusting the angle of the grating, the wavelength of the light that if fed back into the diode can be tuned. Note that both the grating angle and the length of the external cavity are essential to mode selection. Generally, a tilt of the grating changes the cavity length in some arbitrary way that might not be compatible with the wavelength selection of the grating. In the DL 100, the pivot point for the rotation is chosen such that a tilt of the grating to first order also modifies the cavity length such that lasing is maintained. For coarse wavelength adjustements, the grating can be manually tilted using the micrometer screw "5" in the figure. However, for electronic feedback adjustments of the laser and frequency scans, a piezo actuator between the tip of the screw and the grating mount is used.

While a tilt of the grating in the horizontal plan is used to tune the wavelength, the external cavity must be carefully aligned in the vertical direction to ensure that the 1st order diffracted beam finds it way back to the diode. Three set screws "6" are used to align the cavity vertically. During setup, the cavity had to be realigned vertically two times to make the laser work properly again.

4.2.2 Wavemeter setup

For frequency and wavelength measurements we have a laser wavelength meter from Bristol Instruments, Model 621-A, which uses a Michelson interferometer to compare the wavelength of the light to that of an internal, frequency stabilized helium-neon laser. This model measures the absolute wavelength of the laser to an accuracy of $\pm$ 0.2 parts per million, which corresponds to about 200 MHz. While this is not nearly accurate enough to select the right frequency for laser trapping, the wavemeter can place the laser well into the Doppler-broadened absorption profile of an atomic vapor, and puts a narrow atomic resonance within a relatively small frequency scan of the

laser.

The light is coupled into the interferometer via a fiber-optic coupler, which is placed on an optical mount that can have its angles adjusted until one can see its back reflections symmetrically placed apart from the input light. The wavemeter and the fiber operate in visual and near infrared range, allowing us to measure the frequency-doubled probe light at 496 nm, the trap and repumper lasers at 780 nm and the fundamental of the probe laser at 993 nm. Using flip-mounts which can move mirrors reproducably in an out of a beam path, a switchyard is implemented on the table to quickly and conveniently couple all lasers into the wavemeter.

4.2.3 Fabry Perot

A Fabry Perot interferometer as an external cavity can be used to check the longitudinal mode structure of a laser beam. If the finesse is large enough, an upper limit for the laser bandwidth can also be established. The SA200 - Series Scanning Fabry Perot Interferometer from Thorlabs used in this experiment is basically an optical cavity composed of two spherical mirrors separated by a distance equivalent to their radius of curvature r. To understand how a Fabry Perot works one can follow the path of a beam that enters the cavity at a certain height H from its axis. The beams performs a round-trip through paths 1, 2, 3, 4, being reflected back to path 1. The cavity is

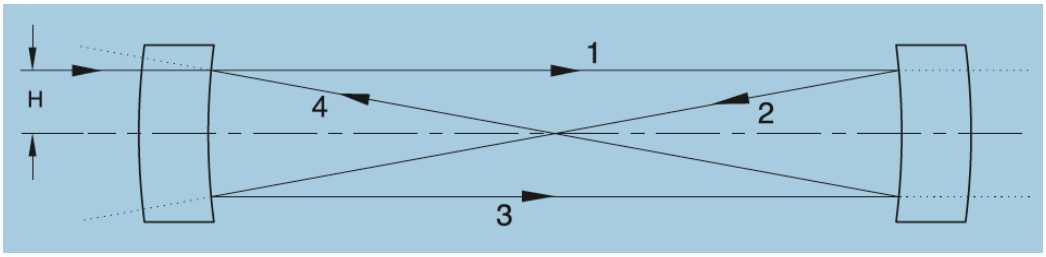

Figure 4.5: Ray trace of an off-axis input ray that traverses the cavity. Figure extracted from Thorlabs manual.

resonant when the total path length the beam travels on a roundtrip is equivalent to

an integer times the light wavelength (when H≠0):

$$m\lambda = 4r. \tag{4.3}$$

The distance between each frequency peak is the rate between the speed of light on air and the length of the round trip. So for a beam well aligned to the cavity axis the free spectral range (FSR) is

$$FSR = \frac{c}{2r}. \tag{4.4}$$

Our Fabry Perot has a FSR of 1 GHz, and a finesse of 300 between 780 and 930 nm. It is still usable at 993 nm, albeit with very low finesse.

4.2.4 Saturation Spectroscopy

Saturation spectroscopy of rubidium vapor was the first method used in this experiment in order to explore the hyperfine structure of this atom and largely eliminate the effects of Doppler broadening caused by the different velocity groups present in the atomic vapor.

With this technique we are able to reduce the broadening of the absorption peaks from approximately 500 MHz (FWHM) to about 20 MHz, somewhat larger than the natural linewidth of 7 MHz.

The principle of saturation spectroscopy is to use two counter-propagating beams of the same frequency in an atomic vapor. The first, a high intensity beam, will saturate the atomic vapor, while the second of low intensity will be measuring absorption. As can be seen in figure 4.6, the beam from the diode laser passes through a glass plate that will reflect approximately 4% of the light in each of its surfaces, then generating two weak parallel beams, the probe and the reference beam. The unreflected portion, the pump beam, just passes through and is reflected off mirrors to counter-propagate with the probe beam in the vapor cell. Unless crossed polarizations are used for the pump and probe beams, they cannot be perfectly collinear while still sending the probe beam to a photodiode. Instead, a small pickup mirror is used to overlap the

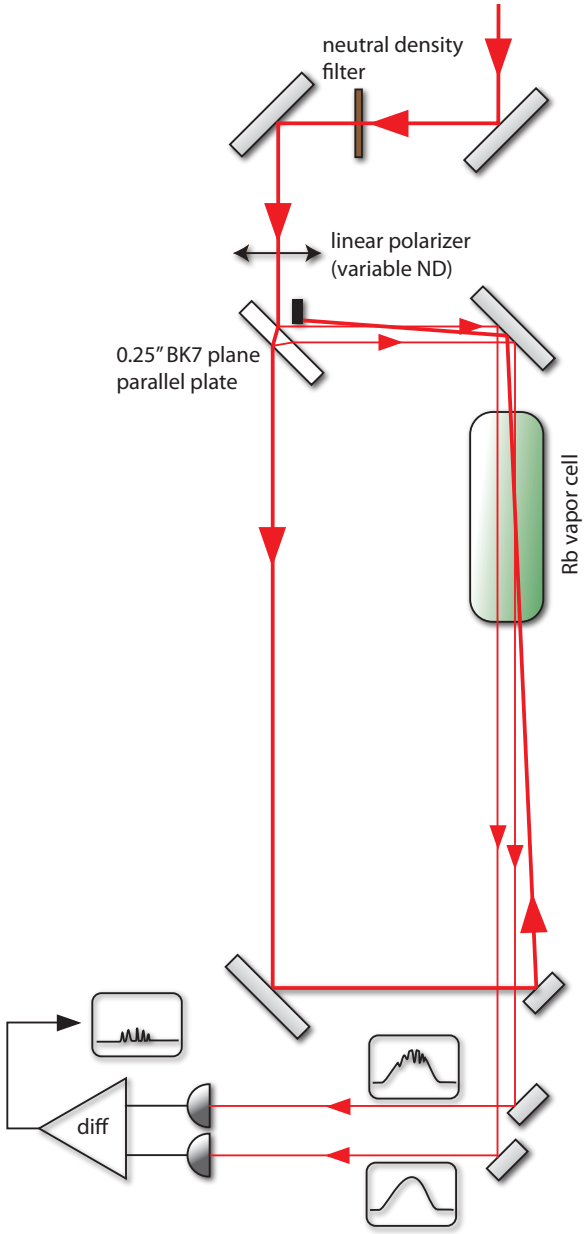

Figure 4.6: Layout of the saturation spectroscopy setup used to monitor the frequency of the trapping laser relative to the D2 line of rubidium.

pump with the probe inside the vapor cell under a very small angle. The detector at the end of the path has two photodiodes that will receive the probe and the reference beams and send their signals to an oscilloscope or a differential amplifier, where the

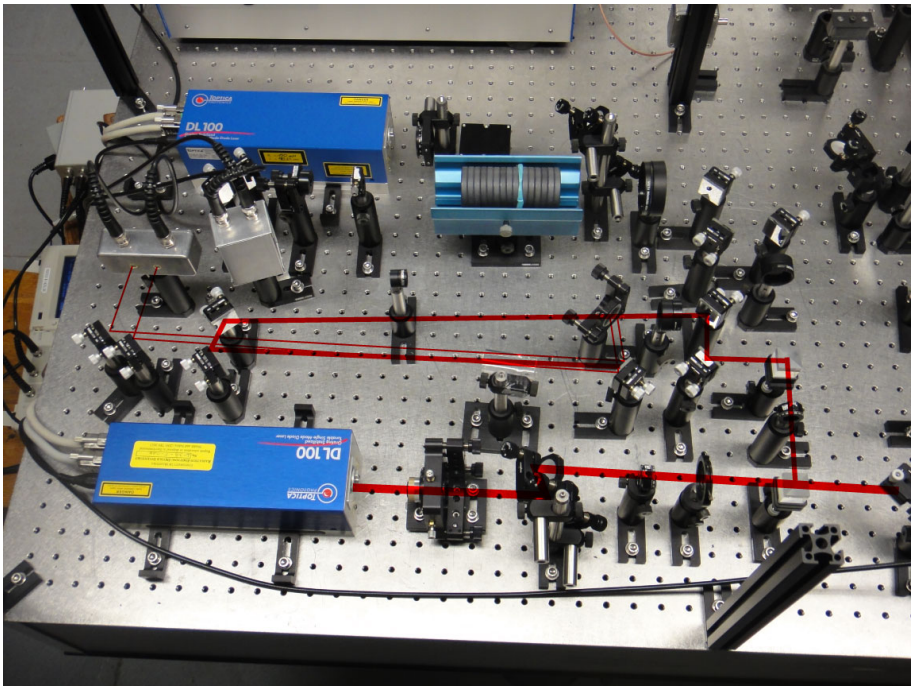

Figure 4.7: Implementation of the saturation spectroscopy setup used to monitor the frequency of the trapping laser relative to the D2 line of rubidium.

transmission of the D_2 lines are going to be monitored.

If the laser frequency is not tuned to the center of the Doppler-broadened atomic resonance, the pump and the probe interact with different velocity classes in the atomic vapor. For example, if the laser is tuned slightly above the atomic resonance, the pump will the get absorbed by atoms moving with a certain velocity along the same direction as the pump beam, and the probe will be absorbed by atoms moving with the same velocity along the direction of the probe beam. Therefore, the absorption of the probe beam is not influenced by the presence of the pump. However, this is not true for the velocity class zero, i.e. atoms that have no velocity component along the direction of the laser beams. I.e. when the laser is tuned to the middle of the Doppler-broadened resonance, the pump and the probe talk tothe same group of atoms. Since the strong pump beam already keeps the atoms excited, the atomic

vapor appear to be transparent to the probe, and the its absorption by the vapor is locally reduced, leading to the Lamb dip, a Doppler-free feature at the line center as shown in figure 4.8.

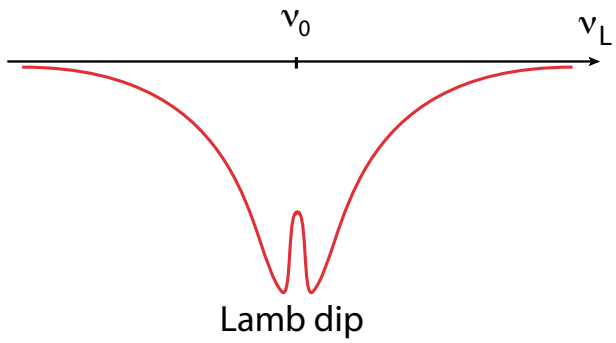

Figure 4.8: Saturation spectroscopy: The Lamb dip.

In a situation where several resonances are closeby (within the envelope of the Doppler profile), additional Lamb dips appear which are called crossover resonances. Saturation can also occur if the pump beam is saturating a velocity group on one transition, and the probe is resonant with the same velocity group on another transition. This always happens if the laser is tuned exactly half-way between the two resonances.

Figure 4.9 shows the level structure and the allowed transitions for the Rb D2 line, for both stable isotopes. From the level separation it is clear that the ground state hyperfine structure will be fully resolved in a vapor cell, whereas the excited state splittings are masked by the Doppler broadening, and will lead to Lamb dips in saturation spectroscopy. The upper panel in figure 4.10 shows this clearly. The uppermost trace shows a simple, Doppler-broadened absorption spectrum. The two outer peak are due to ^{87}Rb, the inner ones stem from ^{85}Rb. The middle trace shows the Doppler profile seen by the probe beam in saturation spectroscopy. Note that due the proximity of the resonances, not all Lamb dips are individually resolved,

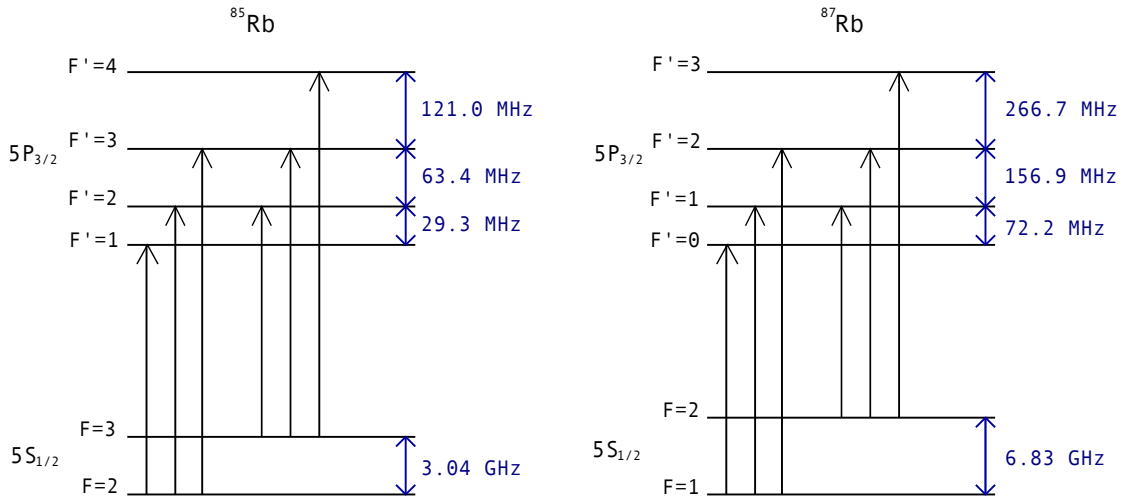

Figure 4.9: Level diagram for the Rb D_2 line

especially for ^{85}Rb. The lower trace illustrates the purpose of the dual weak beam setup: The reference beam, not countered by a pump, records a simple Doppler profile. Subtracting the probe from the reference eliminates the Doppler profile and Lamb dips on a flat background are obtained. In figure 4.11, the Lamb dips are shown in more detail.

4.2.5 DAVLL

In general the external cavity of the laser drifts in frequency due to thermal changes and vibrations (typically tens of MHz per hour). While this can be reduced by placing the laser in an insulated enclosure, it is nevertheless necessary to to stabilize it electronically in feedback loop to the atomic resonance. As discussed earlier, it is relatively straightforward to lock the laser frequency to the peak of an atomic resonance. However, the MOT needs to be stabilized to a frequency about 2 linewidths to the red of the cycling transition in the hyperfine manifold. For this reason we decided to employ a locking scheme that can move the lock point continuously within

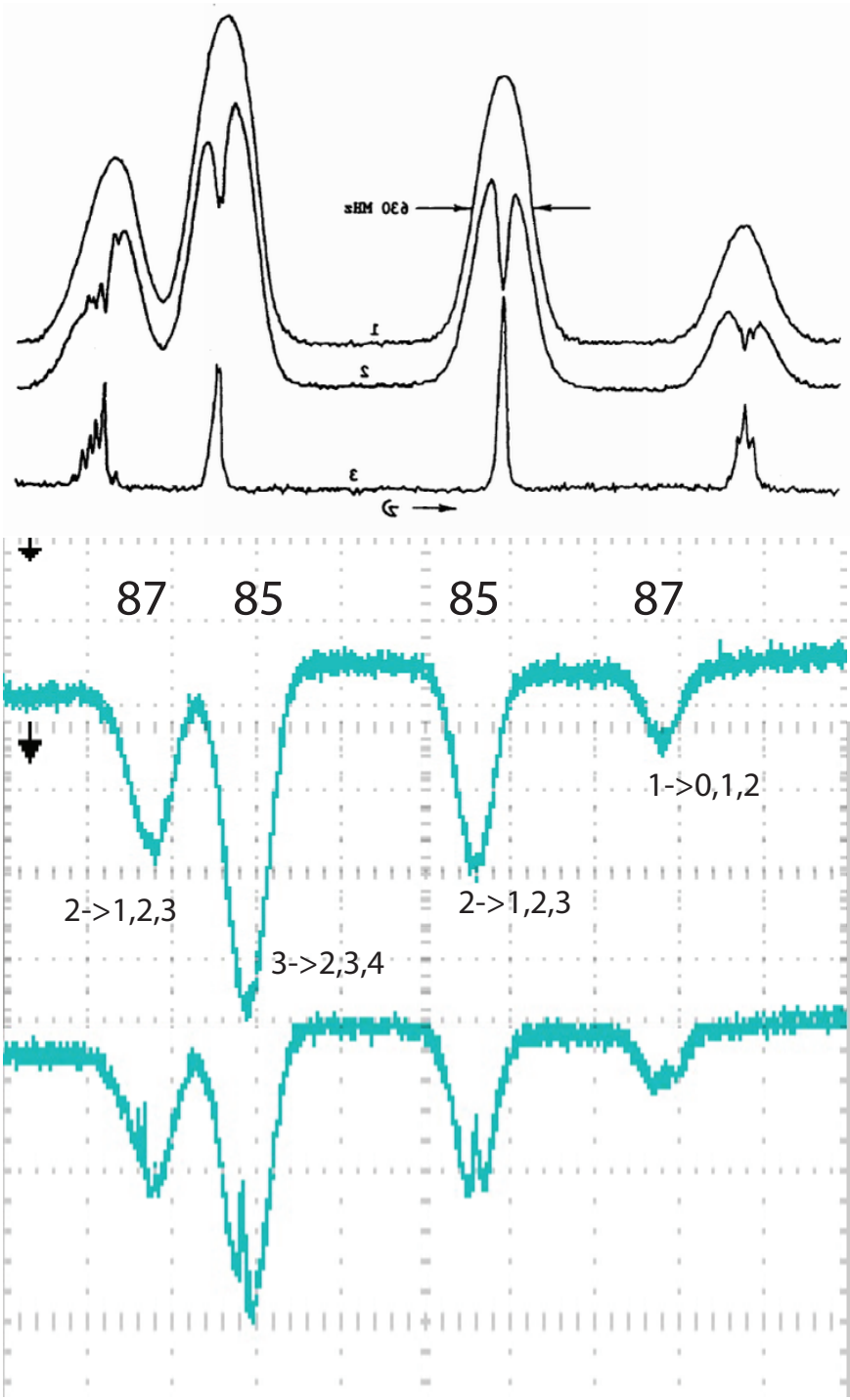

Figure 4.10: Saturation in the Rb D2 line. Upper panel shows the Doppler broadened peak, the saturated absorption and the subtracted signal leaving only the Lamb dips (taken from the MIT lab course manual); note that the plot is mirrored to match the scan direction in the lower panel. Lower panel: Saturation spectroscopy with our trap laser.

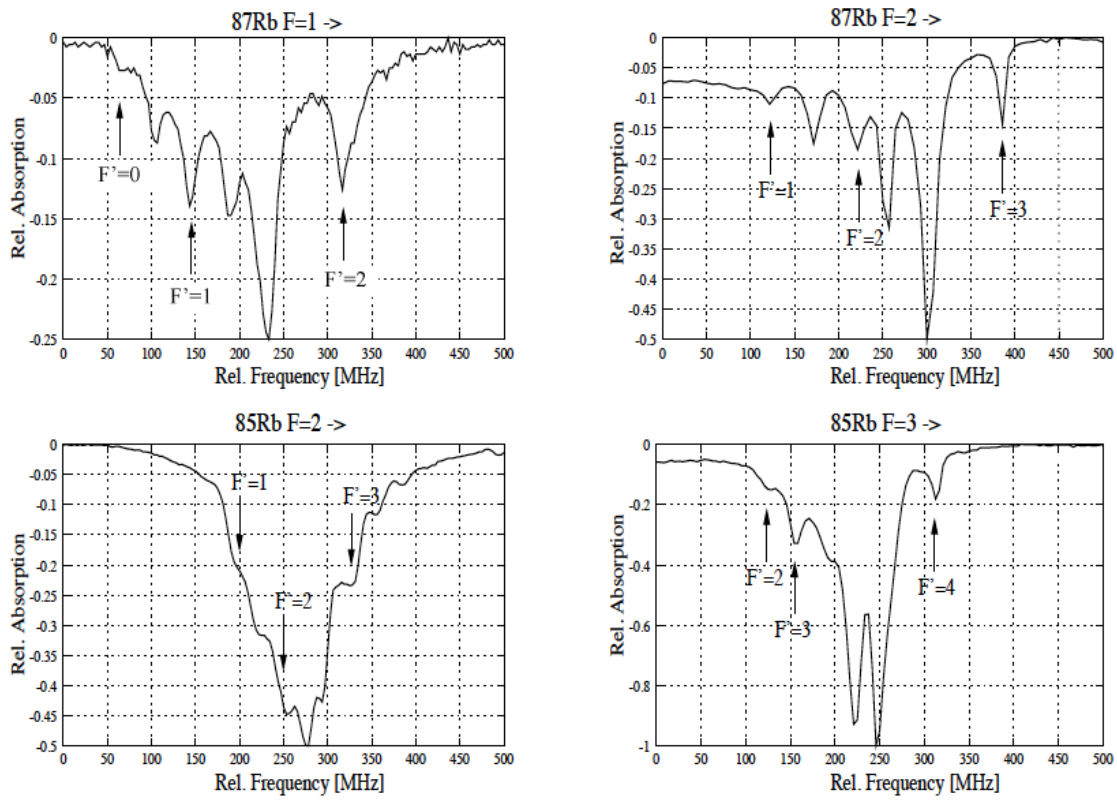

Figure 4.11: Rb D_2 hyperfine transitions. Unlabeled peaks are cross-overs. Taken from [23].

the Doppler profile, known as Dichroic Atomic Vapor Laser Locking (DAVLL) [33].

Figure 4.16 shows schematically our implementation. Linearly polarized from the trap laser is entering the DAVLL setup. An additional linear polarizer is used to ensure that the various reflections off mirrors and beam splitters have not introduced any circularly polarized or unpolarized component, and also serves to reduce the light intensity to a suitable level to avoid saturation of the photodiodes. A Rb vapor cell is enclosed in a stack of circular ring magnets (Master Magnetics, Inc., www.magnetsource.com part # CR162) which produce a reasonably homogenous, longitudinal magnetic field inside the vapor cell [35].

While the light entering the vapor cell is linearly polarized, it is best for the

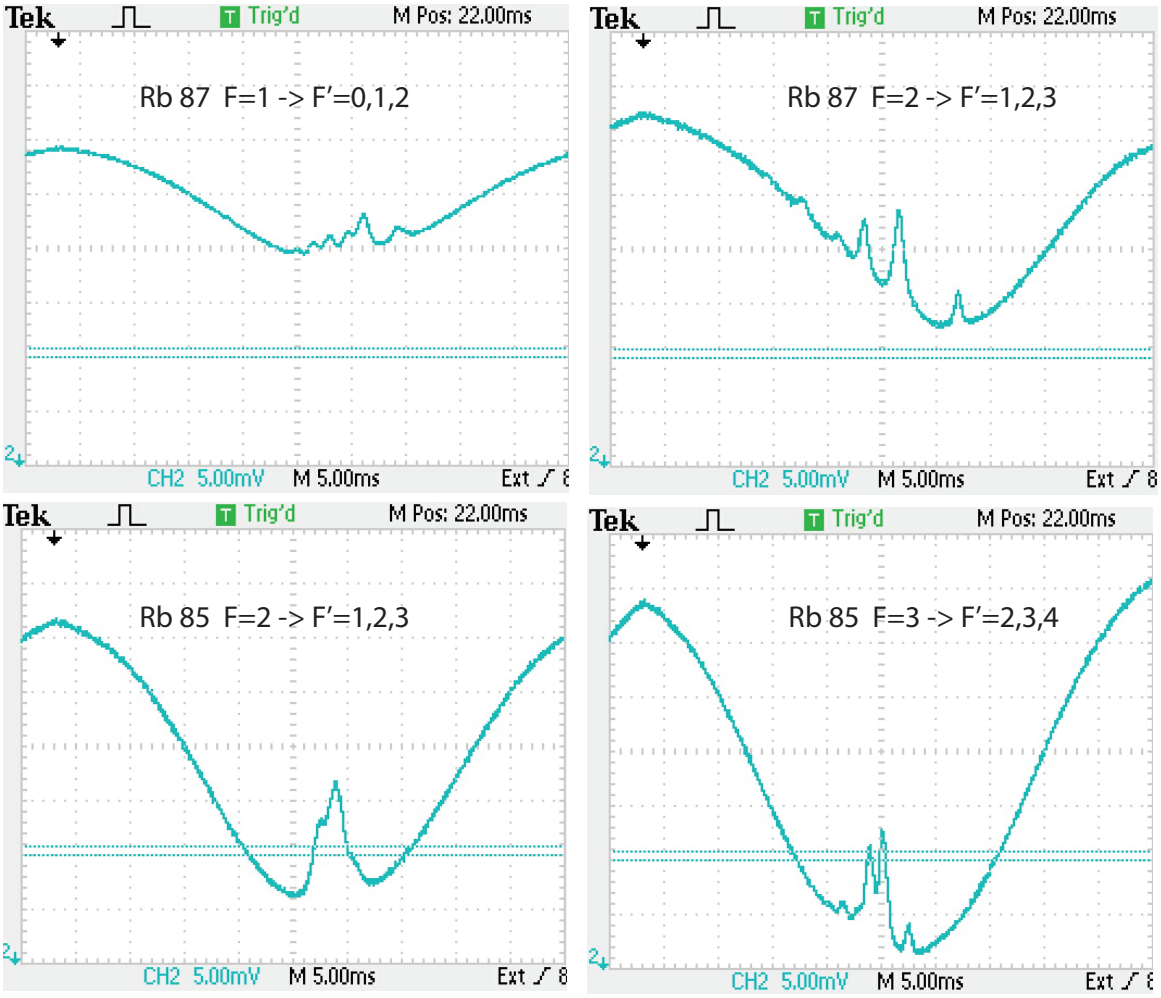

Figure 4.12: Saturation spectroscopy of the Rb D2 resonances using the trap laser setup.

following discussion to think of this light as a 50-50 superposition of left-handed $\sigma-$ and right-handed $\sigma+$ radiation. In the presence of the longitudinal field, $\sigma-$ light drives $\Delta m = -1$ transitions, and $\sigma+$ light $\Delta m = +1$ transitions. The Zeeman effect shifts these transitions in opposite direction from the zero-field location, by about 1.3 MHz per Gauss. After passing the cell, the light enters a quarter-wave plate which will turn the two circular polarizations into linear polarized components perpendicular to each other. By turning the quarter-wave plate, these two orthogonal polarization

components can be aligned such that they are separated in the following Wollaston prism. The separated components, which represent the $\sigma+$ and $\sigma-$ light inside the vapor cell, are sent to photodiodes and subtracted from each other in an amplifier. Figure 4.14 explains the principle behind DAVLL: As a function of frequency, the absorption profiles of $\sigma+$ and $\sigma-$ are shifted with respect to each other symmetrically to the zero-field resonance. If they are electronically subtracted from each other, we obtain the dispersive line shape shown in the lower panel. The zero crossing can be used as a lock point for a feedback system. By misaligning the quarter-wave plate slightly with respect to the Wollaston prism or by amplifying the photodiode signals by different amounts prior to subtraction, the two shifted resonances can acquire somewhat different height, rendering the subtracted signal slightly asymmetric, with a zero crossing shifted away from the zero-field resonance.

The separation between the Doppler profile peaks which were shifted by the Zeeman effect depends on the magnetic field strength, which can vary from ≈ 50 to ≈ 300 Gauss, with wider locking range for values greater than 200 Gauss. The magnetic field must be in the ideal range so that the inclination of the slope is maximum and the broadening of the transitions are minimum, so that the slope does not loose its linearity.

The DAVLL signal is used as a feedback signal generating an error voltage that is applied to the piezo of the external cavity of the laser which shifts the laser to keep the error signal close to zero, and hence locking the diode laser.

This setup offers a robust method for locking and stabilizing a diode laser frequency, not suffering perturbations from external factors as electrical or mechanical fluctuations. The DAVLL locking has numerous advantages over the conventional side-locking method. With the DAVLL setup it is possible to tune the beam over a wide frequency range of about 500 MHz, which is the approximate value of the FWHM from the Doppler profiles shifted by the Zeeman effect. On the other hand the side-locking setup only allows the tuning to a few MHz because the laser is being

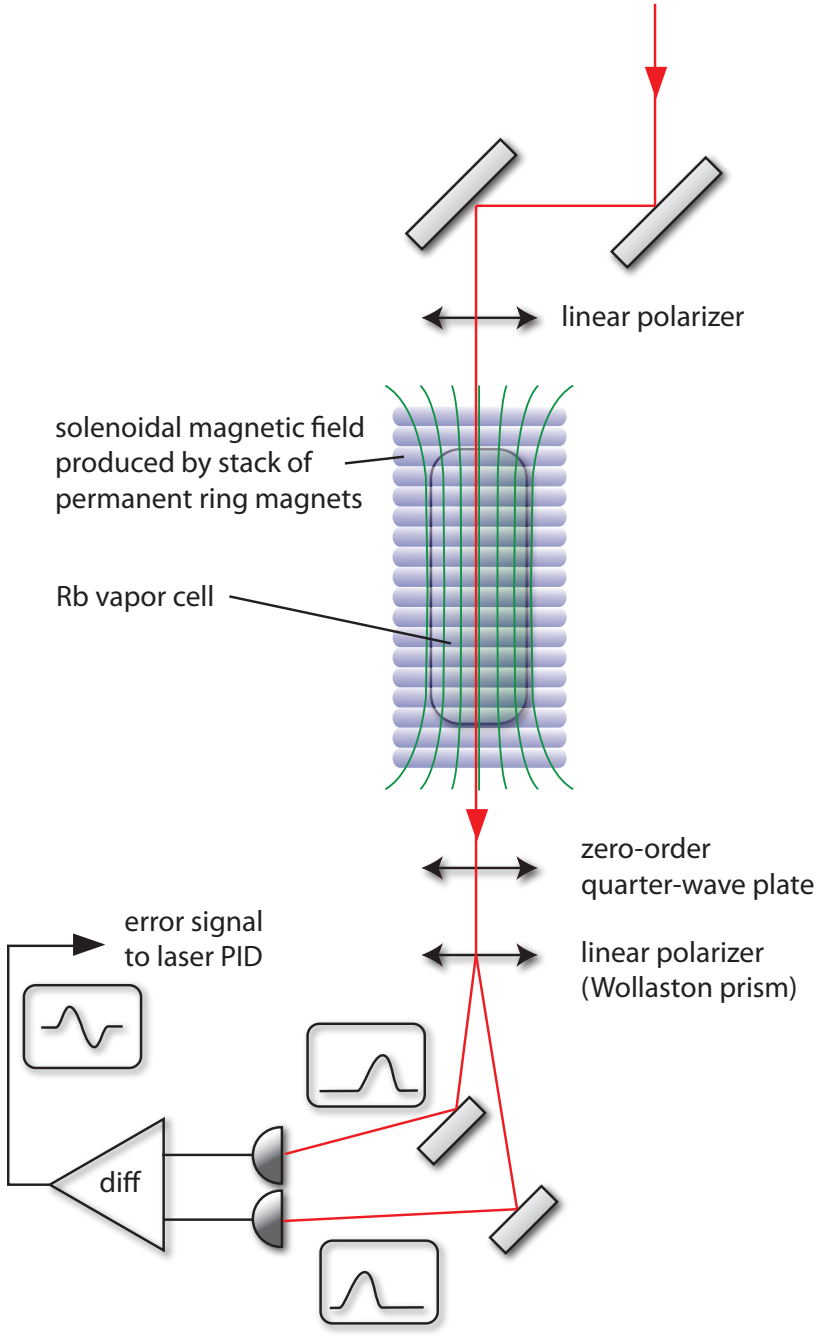

Figure 4.13: Schematic of the DAVLL setup for locking the trap laser.

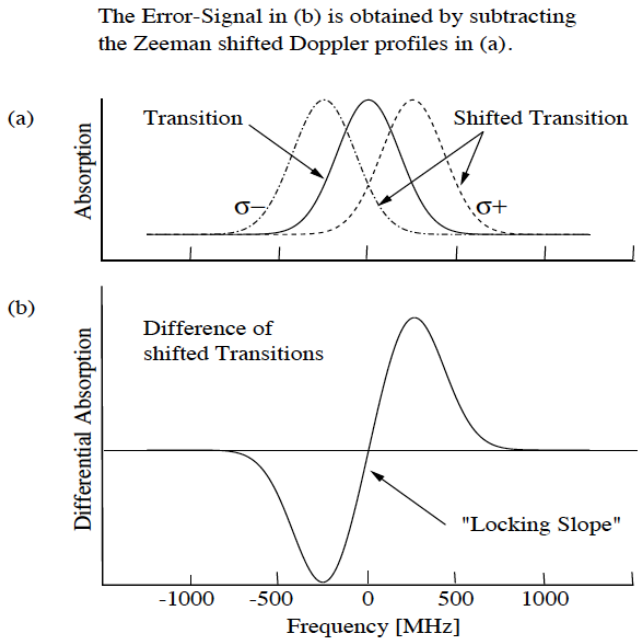

Figure 4.14: Origin of the error-signal. Taken from [23].

locked to the side of a hyperfine peak DAVLL has a low cost and it is simple to build. A more detailed explanation of the DAVLL locking system can be found in reference [23].

The Toptica DL100 laser system does not allow direct input of a piezo control voltage into the SC110 scan module which controls the piezo. However, it accepts a signal on the backplane of the controller crate. We chose to use the Toptica PID module to feed the error signal into the scan module. With appropriate settings of the P,I, and D values, stable locking is achieved reliably.

4.2.6 The MOT

Once the trap laser and repumper beams are merged and expanded, they are fed into the MOT setup. As shown in figure 4.1, the beams must be split up into three with equal intensities, two horizontal and one vertical. Before entering the MOT cell,

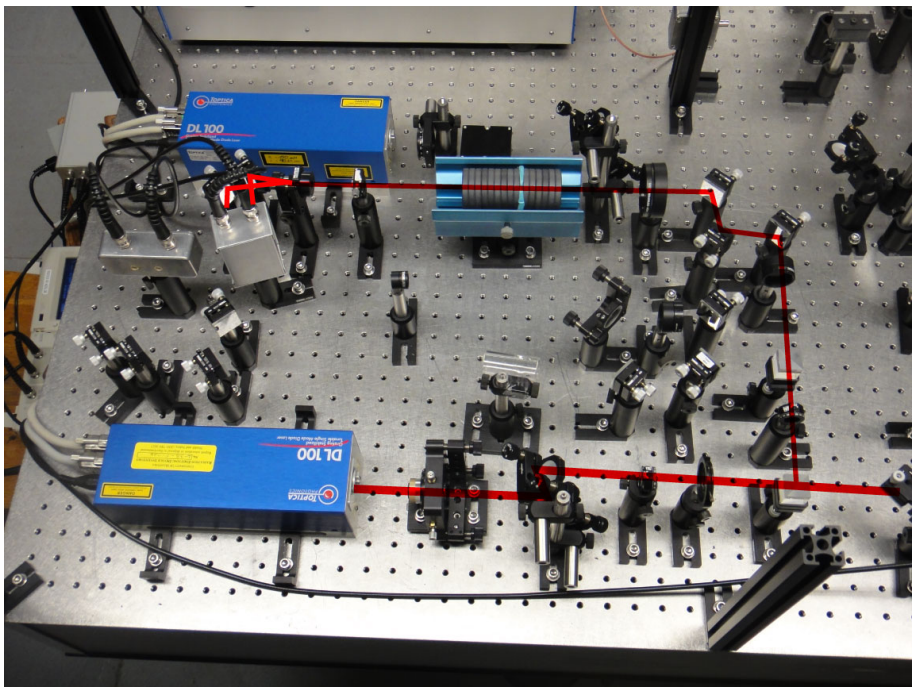

Figure 4.15: Implementation of the DAVLL setup for locking the trap laser.

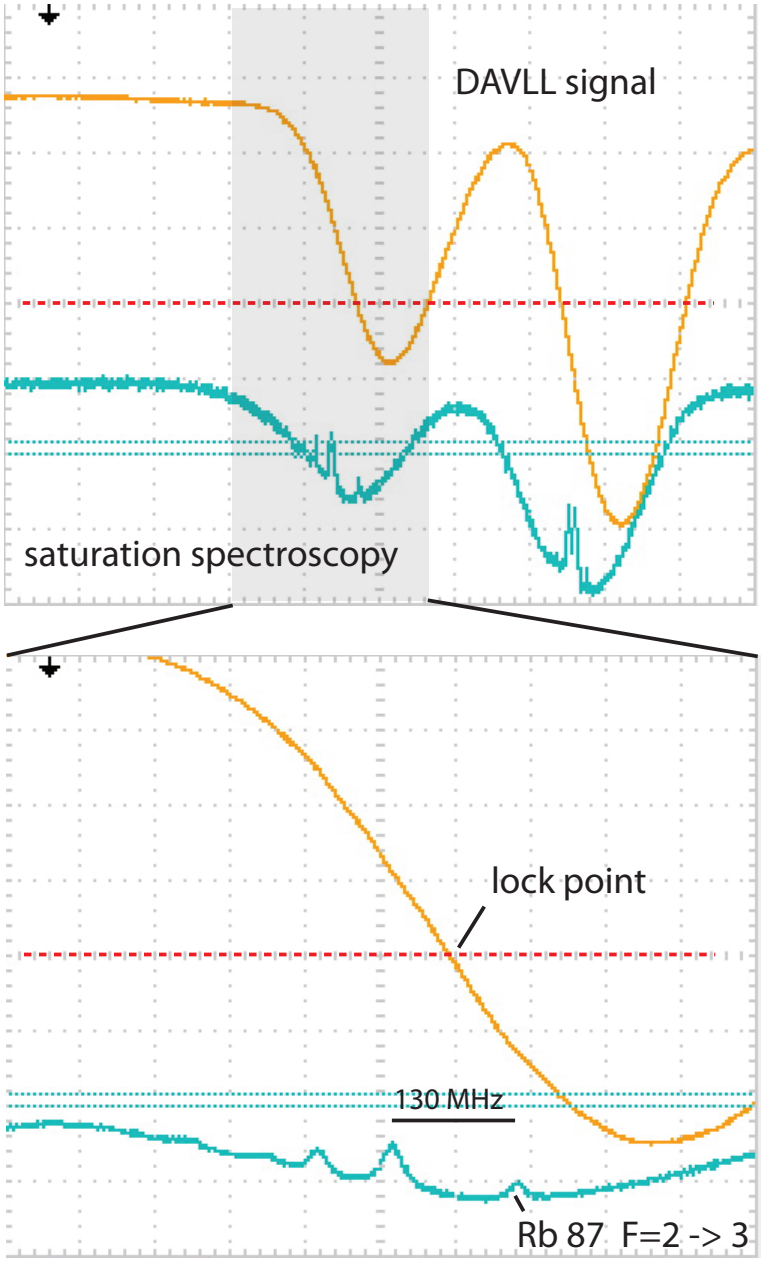

Figure 4.16: DAVLL signal using the trap laser. Due to the proximity of the Doppler broadened resonances, the lineshape of the DAVLL signal deviates significantly from the symmetric shape shown in 4.14.

quarter-wave plates are used to produce circularly polarized light. Each of the three beams is then retro-reflected upon itself. A quarter-wave plate is placed in front of the retro-reflector. As it is passed twice by the light, it effectively acts as a half-wave plate, flipping the rotation direction of the field vector; since the reflection reverses the propagation direction as well, the handedness of the light is preserved, yielding the required $\sigma+ - \sigma-$ configuration required for a MOT. Care has to be taken to give the two horizontal beam identical handedness and the vertical one the opposite handedness due to the geometry of the quadrupole field. The overall sign of the handedness is determined by the sign of the magnetic field. In practice, when trying to establish the MOT, it is most convenient to reverse the polarity of the coil power supply periodically.

4.2.7 Vacuum system

The vapor cell has approximately 10 cm diameter and is coated on the inside with silane coating to prevent alkalis from sticking to the walls (for Rb, this is not necessary as even without the coating, once a monolayer of Rb coats the walls, Rb vapor starts to build up in the cell; however, for a Fr vapor cell MOT, the silane coating is indispensable). The cell is on loan from J. Behr at TRIUMF. The glass cell is attached to a conflat-based UHV vacuum system pumped by a Varian ion getter pump (200 liters/sec). After baking the system can reach a base pressure of well below 10^{-8} mbar. The vacuum system is pumped down from atmospheric pressure using a sorption pump (Varian 941-6501), which can pull a vacuum of around 5×10^{-3} mbar, which is barely enough to get the ion pump started. After the ion pump works sustainably, the sorption pump is valved off from the UHV system. A standard valve (metal bellows against atmosphere and viton seal between the two vacua) did prove insufficient, and an additional all-metal valve was installed.

As a rubidium source, a convenient getter source (SAES Inc. RB/NF/7/25 FT 10+10) was installed on an electric feedthrough in the center cross of the vessel,

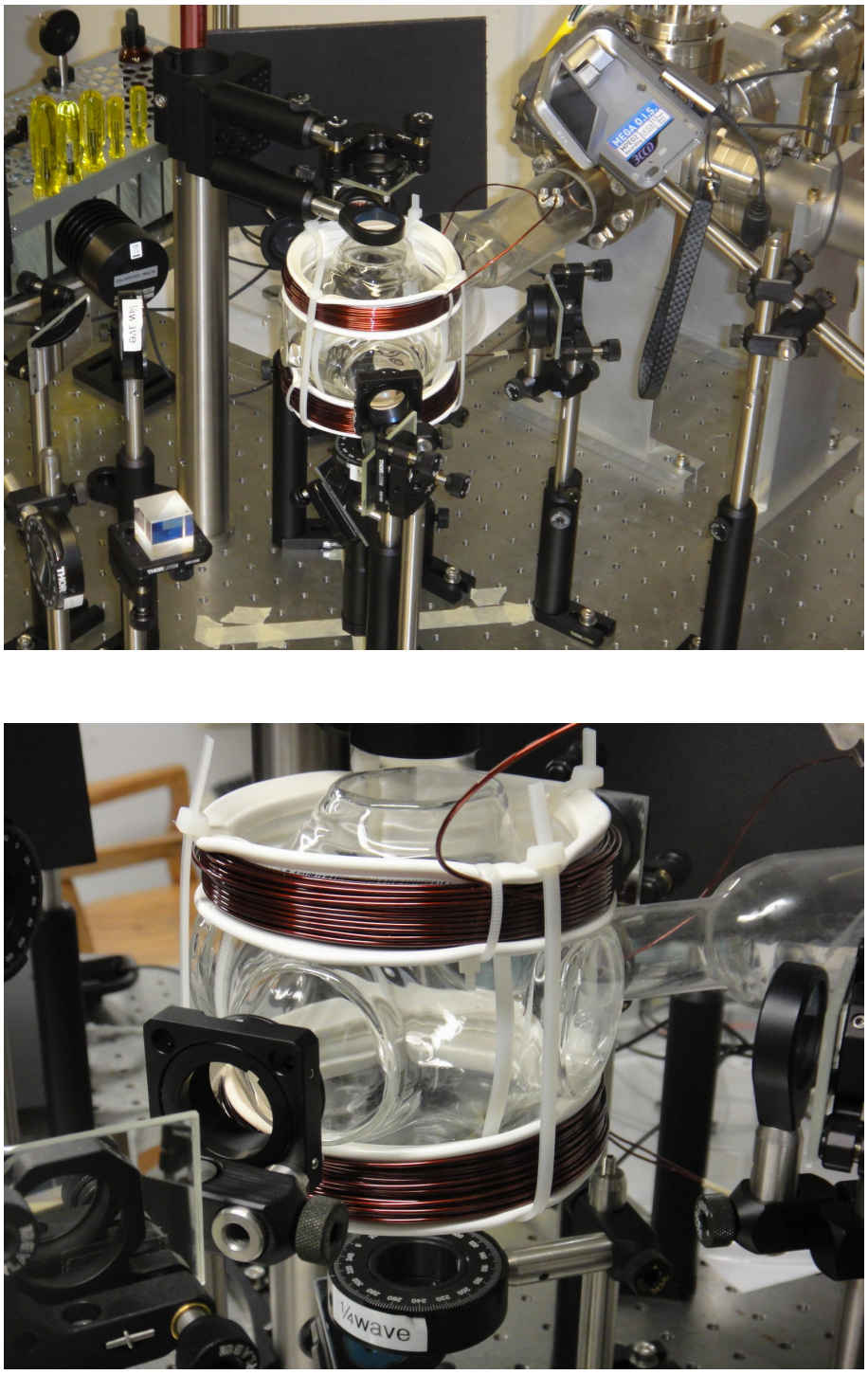

Figure 4.17: Vapor cell MOT.

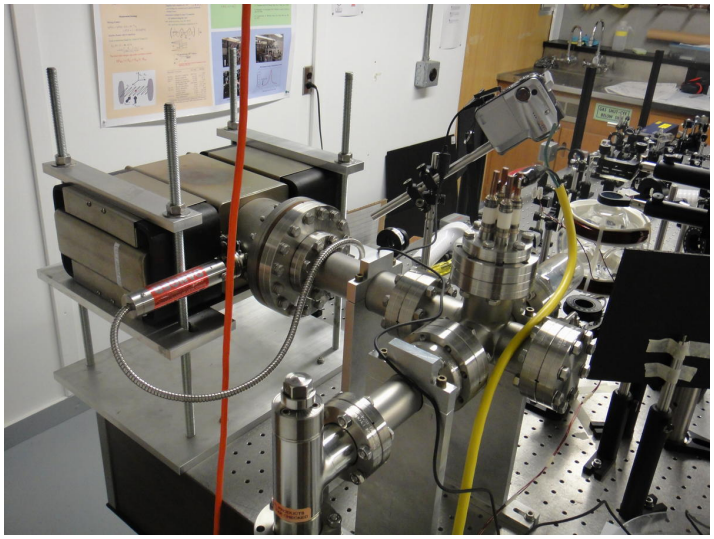

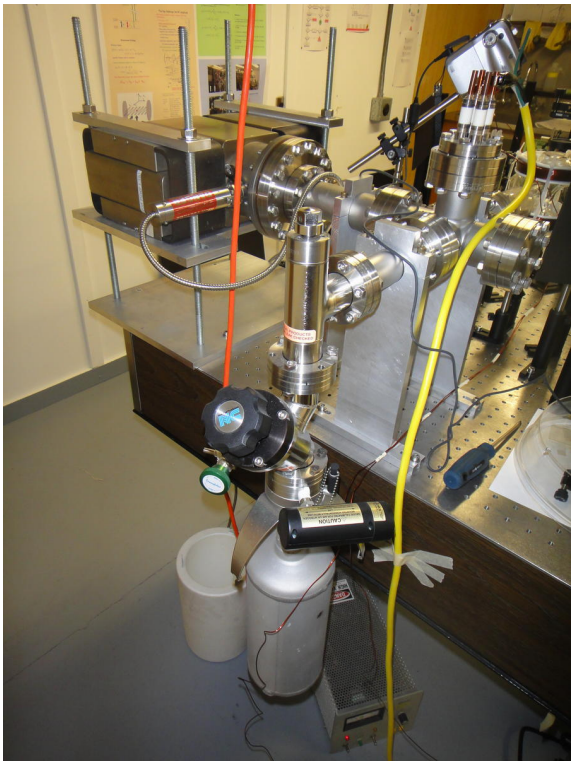

Figure 4.18: UHV system with sorption and ion pumps.

pointing a Rb beam into the vapor cell when activated. As shown in figure **??**, the getter is a strip of metal that contains Rb_2 CrO_4 and a zirconium - aluminum alloy, St101. At room temperature the getter is sealed. Once a current of around 5.3 A is sent through the strip, the resistive heating opens up a crack in the face of the getter and the Rb chromate gets reduced by the St101, producing pure Rb which emanates from the crack. The advantage of these getters is that they can be safely handled in air and that they produce very little gas load when heated.

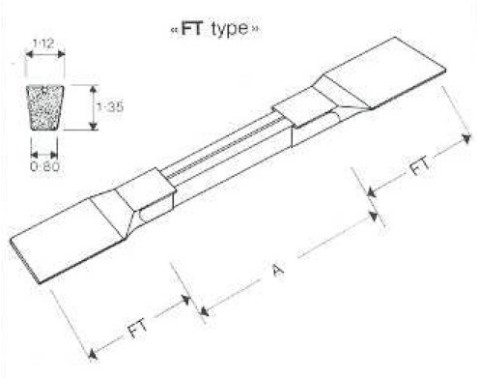

Figure 4.19: Rb getter source; taken from the SAES Inc. Alkali Metal Dispenser catalog.

Chapter 5

CONCLUSIONS AND OUTLOOK

All the components for the MOT have been set up. Currently, work to observe a cold cloud of trapped Rb atoms is under way. Once this is accomplished, the trap will be optimized and the robustness explored and improved. The $5s - 6s$ measurements generaly will require the application of a homogenous electric and magnetic fields. Their implementation is not compatible with the current glass cell vapor MOT. We are in the process of preparing a large stainless steel UHV chamber as a new vacuum chamber for the MOT. It has several large ports that can be used to mount electric field plates and in-vacuum magnetic field coils. This chamber should becomes operational in Fall of 2010. The 5s - 6s probe laser at 496 nm has operated successfully at the required wavelength, but subsequently, the doubling stage failed to produce blue output. We are currently re-aligning the system, and light should be available before the new chamber is ready to take beam.

TRIUMF has conducted first tests with their actinide target in late 2009, and francium production was demonstrated. In 2011, a Fr trapping facility will be established on the floor of the ISAC hall.

Appendix A

MAPLE CODE FOR THE CHARACTERIZATION OF THE $S \rightarrow S$ TRANSITION

A code was developed in Maple 11 to calculate all the relevant amplitudes and rates in alkali $ns \rightarrow n's$ transitions. It calculates the C-coefficients which are introduced in Gilbert's thesis [24] explicitly for ^{133}Cs, for any alkali isotope, i.e. nuclear spin. In the future, this code will be used to evaluate transition rates for experiments in various geometries. Attached is a Maple sample session.

Maple program to calculate amplitudes and rates in alkali ns -> n's transitions.

G. Gwinner, S. Toews, C. de Oliveira 2008-2010
C-coefficient calculation, 6j symbols by S. Toews

Setting up

Technical definitions, general remarks

> All quantities in SI units carry the suffix _SI (and must be in basic SI units, no nanometer etc), quantities without such a suffix are in atomic units, quantities other units or non-standard SI (e.g. V/cm) must be labelled with an explicit suffix such as E_stark_V_per_cm

```
> restart; with(LinearAlgebra): #with(StringTools):
> printlevel:=3;
```

printlevel := 3

```
> algebra:=false;
```

Choose algebraic or numerical result.

algebra := *false*

Implements a Kronecker delta function.

```
> delta:= proc(aa,bb)
  if not type(aa - bb, numeric) then RETURN('procname(args)')
  fi;
  if (aa = bb) then 1 else 0 fi;
  end proc;
```

δ := **proc**(*aa*, *bb*)
if not *type*(*aa* − *bb*, *numeric*) **then** *RETURN*('*procname*(*args*)') **end if**;
if *aa* = *bb* **then** 1 **else** 0 **end if**
end proc

Unit vectors.

```
> x:=<1,0,0>: y:=<0,1,0>: z:=<0,0,1>:
```

Variables

```
> Isotope:=4;
```

1: Rb85 2: Rb 87 3: Cs133 4: Fr210

Isotope := 4

```
> F1:=Inuc-1/2; F2:=Inuc-1/2;
```

F1: lower n state, F2: higher n state. **Note:** this might be abolished later on, eventually the code should not be limited to just one particular transition, everything should be set up in general (i.e. a given isotope) and then specifics (F1,F2,m1,m2,laserdirection) are

specified as needed in the actual calculations

$$F1 := Inuc - \frac{1}{2}$$

$$F2 := Inuc - \frac{1}{2}$$

```
> Estark_V_per_cm:=2000;
```
Stark field in V/cm; 450-950 V/cm for Wood et al.

$$Estark\_V\_per\_cm := 2000$$

```
> r:=1;
```
Elliptical polarization ratio eps-x/eps-z or cot(theta); r=0 gives linear polarization in z-direction; Wood uses r=1,2; note: k is always in y-direction

$$r := 1$$

```
> Plaser_SI:=0.2;
```
Total power of laser in W (for diameter of 0.41mm and 30000 powerbuildup, use 36mW here).

$$Plaser\_SI := 0.2$$

```
> powerbuildup:=1;
```
Power buildup in cavity (30000 for Wood, 1 for a single unreflected beam).

$$powerbuildup := 1$$

```
> laserdiam_SI:=1.00/1000;
```
Diameter of laser in m (waist 0.41mm for Wood). ENTER VALUE AS (diameter in mm)/1000.

$$laserdiam\_SI := 0.001000000000$$

```
> laserdirection:=1;
```
Laser beam direction is fixed in this setup to be along the y-axis; chose either propagation in positive direction (+1) or negative (-1)

$$laserdirection := 1$$

Physics definitions (Rb85, Rb87, Cs133, Fr210), add new isotopes here

Conversion between SI and atomic units (S2A = S.I. to a.u.; A2S = a.u. to S.I.)

```
> EF_S2A:= 1.944690567144141*1e-12; EF_A2S:= 1/EF_S2A;
```
Electric field in V/m to a.u.

$$EF\_S2A := 1.944690567\ 10^{-12}$$

$$EF\_A2S := 5.142206256\ 10^{11}$$

```
> time_S2A := 4.134137337414122*1e16; time_A2S:=
  1/time_S2A;
```
Time in s to a.u.

$$time\_S2A := 4.134137337\ 10^{16}$$

$$time\_A2S := 2.418884325\ 10^{-17}$$

```
> Laser_I_S2A:= 5.548225828243671/(1.889726133921252*1e10)
```

```
^2; Laser_I_A2S:= 1/Laser_I_S2A;
```
#Laser intensity to au (used conversion for W/m^2 by W and m)

$$Laser\_I\_S2A := 1.553661455\ 10^{-20}$$

$$Laser\_I\_A2S := 6.436408632\ 10^{19}$$

```
> rate_S2A:=time_A2S; rate_A2S:=time_S2A;
```
rate (events per time unit) conversion

$$rate\_S2A := 2.418884325\ 10^{-17}$$

$$rate\_A2S := 4.134137337\ 10^{16}$$

Constants

General constants

```
> c_SI:=299792458; c:=137.0359996287515; mu_B:=0.5;
epsilon_0:=0.07957747154594767;
```
#Speed of light in S.I.; speed of light, Bohr magneton and permittivity in a.u..

$$c\_SI := 299792458$$

$$c := 137.0359996287515$$

$$\mu B := 0.5$$

$$\varepsilon 0 := 0.07957747154594767$$

Atom specific

```
> alpha_vec:=[235.96,235.96,268.6,375.3];
```
scalar transition polarizability alpha in a.u.

$$\alpha vec := [235.96, 235.96, 268.6, 375.3]$$

```
> beta_vec:=[9.22,9.22,26.85,73.23];
```
tensor transition polarizabilities beta in a.u.

$$\beta vec := [9.22, 9.22, 26.85, 73.23]$$

```
> #DeltaF:=F2-F1;
```
eventually will be defined in the calculations section as needed

```
> hfs_lo_vec:=[3.3e9,6.834682610904299e9,9.193e9,
46.768e9];
```
Hyperfine splitting of the lower s-state in Hz (nu)

$$hfs\_lo\_vec := [3.3\ 10^{9}, 6.834682610904299\ 10^{9}, 9.193\ 10^{9}, 4.6768\ 10^{10}]$$

```
> hfs_hi_vec:=[717.541e3,1615.3216e3,2.185e9,10.256e9];
```
Hyperfine splitting of the higher s-states in Hz (nu).

$$hfs\_hi\_vec := [7.17541\ 10^{5}, 1.6153216\ 10^{6}, 2.185\ 10^{9}, 1.0256\ 10^{10}]$$

```
> Inuc_vec:=[5/2,3/2,7/2,6];
```
nuclear spin of isotopes

$$Inuc\_vec := \left[\frac{5}{2}, \frac{3}{2}, \frac{7}{2}, 6\right]$$

```
> lambda_SI_vec:=[496,496,540,506]*1e-9;
```
Wavelength of the s-s transition

$$\lambda SI\_vec := [4.96\ 10^{-7}, 4.96\ 10^{-7}, 5.40\ 10^{-7}, 5.06\ 10^{-7}]$$

```
> mrel_vec:=[n,n,-42.1e-6,46.1e-5];
```

Relativistic M1 amplitude, a.u. times muB.

$$mrel\_vec := [n,\ n,\ -0.0000421,\ 0.000461]$$

```
> tau_SI_vec:=[45.6e-9,45.6e-9,53e-9,53.3e-9];
```

radiative lifetime of the upper s state

$$\tau SI\_vec := [4.56\ 10^{-8},\ 4.56\ 10^{-8},\ 5.3\ 10^{-8},\ 5.33\ 10^{-8}]$$

Experimental geometry

```
> Estark_SI:=Estark_V_per_cm*100;
```

simple conversion from V/cm to V/m

$$Estark\_SI := 200000$$

```
> khat:=<0,laserdirection,0>;
```

Define propagation direction of laser field; it is always along the y-axis; the laser direction is considered the definition of the y-axis, x and y are nominally defined by the external E and B fields and the laser polarization, but could have slight misalignments, which will be considered as part of the error analysis. **Note:** this might have to be changed, since we will want to consider both laser directions (ie. power buildup cavity).

$$khat := \begin{bmatrix} 0 \\ 1 \\ 0 \end{bmatrix}$$

Algebra/not algebra *(might not be consistent yet, but for now, numeric evaluation is first goal)*

```
> # first some definitions that would be used if atomic constants and fields are not evaluated numerically; if numerical evaluation is chosen (algebra=false), these initial definitions will be overwritten in the following if-section with numerical values
```

```
> Estark:=<Estx,Esty,Estz>;
```

generic external electric field, it could be further specified if a certain geometry is chosen (<Estx,0,0> for example)

$$Estark := \begin{bmatrix} Estx \\ Esty \\ Estz \end{bmatrix}$$

```
> if (algebra=true) then unassign('r') end if;
```

leave 'r' symbolic, if algebraic evaluation

```
> eps:=eps_sc*<I*r/sqrt(1+r^2),0,1/sqrt(1+r^2)>;
```

unit polarization vector

$$eps := \begin{bmatrix} \frac{1}{2}\,\mathrm{I}\,eps\_sc\sqrt{2} \\ 0 \\ \frac{1}{2}\,eps\_sc\sqrt{2} \end{bmatrix}$$

```
> B:=khat &x eps;
```

#Laser B-field = cross product (k x epsilon) for M1 amplitude. k is the laser propagation direction, perpendicular to the polarization. **Note:** the externally applied

static B-field will be labelled **Bext**.

$$B := \begin{bmatrix} \frac{1}{2}\, eps\_sc\sqrt{2} \\ 0 \\ -\frac{1}{2}\, \mathrm{I}\, eps\_sc\sqrt{2} \end{bmatrix}$$

the "if not algebra" section

```
> if not algebra then
```
#These are left out if algebraic result is desired. In that case, alpha etc. will remain symbolic.
```
> alpha:=alpha_vec[Isotope];
> beta:=beta_vec[Isotope];
> Inuc:=Inuc_vec[Isotope];
> tau:=tau_SI_vec[Isotope]*time_S2A;
> Estark:=<Estark_SI,0,0>*EF_S2A;
```
#Stark field convert E to au. In Wood et al. E is in x-direction.
```
> Laser_I_SI:=evalf(powerbuildup*Plaser_SI/(Pi*
(laserdiam_SI/2)^2));
```
Laser intensity in W/m^2, should be 8e9 for Wood
```
> Mhf:=(F1-F2)*sqrt(hfs_lo_vec[Isotope]*hfs_hi_vec
[Isotope])/(c_SI/(lambda_SI_vec[Isotope]))*mu_B;
> Mrel:=mrel_vec[Isotope]*mu_B;
```
#Spin independent M1 amplitude in atomic units, for Cs. Page 115 Gilbert: M= -29.73*beta Mhf = 5.35*Beta.
```
> Mtot:=Mrel+Mhf;
```
M1 amplitude from p.104 Gilbert
```
> eps_sc:=sqrt(754*Laser_I_SI)*EF_S2A;
```
Laser electric field in a.u. for laser intensity in W/m^2. from Saleh & Teich (1st edition), I = eps^2/(2*377 Ohms), i.e. eps^2 = 754 Ohms * I
```
> #epsZ:=eps_scalar/(sqrt(1+r^2));
```
z component of laser electric field, in terms of ellipt. pol. param. r
```
> #eps:=<I*r*epsZ,0,epsZ>;
```
Complex polarization, with the magnitude of the laser electric field
```
> end if;
```

$$\alpha := 375.3$$

$$\beta := 73.23$$

$$Inuc := 6$$

$$\tau := 2.203495201\ 10^{9}$$

$$Estark := \begin{bmatrix} 3.889381134000000006\ 10^{-7} \\ 0. \\ 0. \end{bmatrix}$$

$$Laser\_I\_SI := 2.546479089\ 10^{5}$$

$$Mhf := 0.$$

$$Mrel := 0.0002305$$

$$Mtot := 0.0002305$$

$$eps\_sc := 2.694674035\ 10^{-8}$$

```
> eps;
```

$$\begin{bmatrix} \frac{1}{2}\, I\, eps\_sc\sqrt{2} \\ 0 \\ \frac{1}{2}\, eps\_sc\sqrt{2} \end{bmatrix}$$

C-coefficients *(use only ccoeff(F1,F2,m1,m2,Inuc) outside of this section)*

```
> ccoeff:=proc(F1,F2,m1,m2,Inuc)
  #a wrapper function that calls Cgil(deltaF,q) to use a notation as used in the literature
> if (abs(F1-F2)>1) then 0
> elif (abs(m1-m2)>1) then 0
> else simplify(eval(subs({F_1=F1,m_2=m2,I_nuc=Inuc},Cgil
  (F2-F1,m2-m1))))
  #The variables that are not part of the parameters of Cgil must be substituted into the
  expression, if F2-F1 and/or m2-m1 are out of bounds (beyond a change of 1), zero is
  returned. Cgil is now defined such that the variables used in it  are not used anywhere
  else in the code to make sure that it is only using the values given as input via the
  procedure "ccoeff".
> end if;
> end proc;
```

```
ccoeff := proc(F1, F2, m1, m2, Inuc)
    if 1 < abs(F1 - F2) then
        0
    elif 1 < abs(m1 - m2) then
        0
    else
        simplify(eval(subs({F_1 = F1, m_2 = m2, I_nuc = Inuc}, Cgil(F2 - F1,
        m2 - m1))))
    end if
end proc
```

```
> # Do not use F_1,F_2,m_1,m_2,I_nuc anywhere else in the program, and do not use
  "Cgil" directly, but always call the function "ccoeff(F1,F2,m1,m2,Inuc)"
> Cgil(-1,-1):=1/48*(-1)^(2*F_1+2*I_nuc)*(12*F_1+6)^(1/2)*
  6^(1/2)*(-(2*I_nuc+2*F_1+3)*(2*F_1+2*I_nuc-1)*(2*I_nuc-2*
  F_1+3)*(2*I_nuc-2*F_1-1)/F_1/(4*F_1^2-1))^(1/2)*((F_1+1+
  m_2)*(F_1+m_2)/F_1/(2*F_1+1))^(1/2);
```

$$Cgil(-1, -1) := \frac{1}{48}\,(-1)^{2F\_1}$$

$$+ 2\,I\_nuc\sqrt{12\,F\_1 + 6}\,\sqrt{6}\left(-\frac{1}{F\_1\left(4\,F\_1^2 - 1\right)}\left((2\,I\_nuc\right.\right.$$

$$\left.\left. + 2\,F\_1 + 3\right)\left(2\,F\_1 + 2\,I\_nuc - 1\right)\left(2\,I\_nuc - 2\,F\_1 + 3\right)\left(2\,I\_nuc - 2\,F\_1\right.\right.$$

$$-1)))^{1/2}\sqrt{\frac{(F\_I+1+m\_2)\,(F\_I+m\_2)}{F\_I\,(2\,F\_I+1)}}$$

```
> Cgil(-1,0):=1/24*(-1)^(2*I_nuc+2*F_1+1)*(12*F_1+6)^(1/2)*
  6^(1/2)*(-(2*I_nuc+2*F_1+3)*(2*F_1+2*I_nuc-1)*(2*I_nuc-2*
  F_1+3)*(2*I_nuc-2*F_1-1)/F_1/(4*F_1^2-1))^(1/2)*(1/F_1/
  (2*F_1+1)*(F_1^2-m_2^2))^(1/2);
```

$$Cgil(-1,0) := \frac{1}{24}\,(-1)^{2\,I\_nuc+2\,F\_I+1}\sqrt{12\,F\_I+6}\,\sqrt{6}\left(-\frac{1}{F\_I\,(4\,F\_I^2-1)}((2\,I\_nuc+2\,F\_I+3)\,(2\,F\_I+2\,I\_nuc-1)\,(2\,I\_nuc-2\,F\_I+3)\,(2\,I\_nuc-2\,F\_I-1))\right)\sqrt{\frac{F\_I^2-m\_2^2}{F\_I\,(2\,F\_I+1)}}^{1/2}$$

```
> Cgil(-1,1):=1/48*(-1)^(2*F_1+2*I_nuc)*(12*F_1+6)^(1/2)*6^
  (1/2)*(-(2*I_nuc+2*F_1+3)*(2*F_1+2*I_nuc-1)*(2*I_nuc-2*
  F_1+3)*(2*I_nuc-2*F_1-1)/F_1/(4*F_1^2-1))^(1/2)*((F_1-
  m_2)*(F_1+1-m_2)/F_1/(2*F_1+1))^(1/2);
```

$$Cgil(-1,1) := \frac{1}{48}\,(-1)^{2\,F\_I+2\,I\_nuc}\sqrt{12\,F\_I+6}\,\sqrt{6}\left(-\frac{1}{F\_I\,(4\,F\_I^2-1)}((2\,I\_nuc+2\,F\_I+3)\,(2\,F\_I+2\,I\_nuc-1)\,(2\,I\_nuc-2\,F\_I+3)\,(2\,I\_nuc-2\,F\_I-1))\right)\sqrt{\frac{(F\_I-m\_2)\,(F\_I+1-m\_2)}{F\_I\,(2\,F\_I+1)}}^{1/2}$$

```
> Cgil(0,-1):=1/48*(-1)^(2*F_1+2*I_nuc)*(12*F_1+6)^(1/2)*
  (4*I_nuc^2+4*I_nuc-4*F_1^2-4*F_1-3)*6^(1/2)*((F_1+1+m_2)*
  (F_1-m_2)/F_1/(F_1+1))^(1/2)/(F_1*(2*F_1+1)*(F_1+1))^
  (1/2);
```

$$Cgil(0,-1) := \frac{1}{48}\,\frac{1}{\sqrt{F\_I\,(2\,F\_I+1)\,(F\_I+1)}}\left((-1)^{2\,F\_I+2\,I\_nuc}\sqrt{12\,F\_I+6}\,(4\,I\_nuc^2+4\,I\_nuc-4\,F\_I^2-4\,F\_I-3)\,\sqrt{6}\,\sqrt{\frac{(F\_I+1+m\_2)\,(F\_I-m\_2)}{F\_I\,(F\_I+1)}}\right)$$

```
> Cgil(0,0):=1/24*(-1)^(2*F_1+2*I_nuc)*(12*F_1+6)^(1/2)*(4*
  I_nuc^2+4*I_nuc-4*F_1^2-4*F_1-3)*6^(1/2)*m_2/(F_1*(2*
  F_1+1)*(F_1+1))^(1/2)/(F_1*(F_1+1))^(1/2);
```

$$Cgil(0,0) := \frac{1}{24}\left((-1)^{2\,F\_I+2\,I\_nuc}\sqrt{12\,F\_I+6}\,(4\,I\_nuc^2+4\,I\_nuc-4\,F\_I^2-4\,F\_I-3)\,\sqrt{6}\,m\_2\right)\Big/\left(\sqrt{F\_I\,(2\,F\_I+1)\,(F\_I+1)}\,\sqrt{F\_I\,(F\_I+1)}\right)$$

```
> Cgil(0,1):=1/48*(-1)^(2*I_nuc+2*F_1+1)*(12*F_1+6)^(1/2)*
```

```
(4*I_nuc^2+4*I_nuc-4*F_1^2-4*F_1-3)*6^(1/2)*((F_1+m_2)*
(F_1+1-m_2)/F_1/(F_1+1))^(1/2)/(F_1*(2*F_1+1)*(F_1+1))^
(1/2);
```

$$Cgil(0,1) := \frac{1}{48}\,\frac{1}{\sqrt{F\_1\,(2\,F\_1+1)\,(F\_1+1)}}\left((-1)^{2\,I\_nuc+2\,F\_1}\right.$$

$$+1\sqrt{12\,F\_1+6}\,\left(4\,I\_nuc^2+4\,I\_nuc-4\,F\_1^2-4\,F\_1\right.$$

$$\left.\left.-3\right)\sqrt{6}\,\sqrt{\frac{(F\_1+m\_2)\,(F\_1+1-m\_2)}{F\_1\,(F\_1+1)}}\right)$$

```
> Cgil(1,-1):=1/48*(-1)^(2*I_nuc+2*F_1+1)*(12*F_1+6)^(1/2)*
6^(1/2)*(-(2*I_nuc+2*F_1+5)*(2*I_nuc+2*F_1+1)*(2*I_nuc-2*
F_1+1)*(2*I_nuc-2*F_1-3)/(2*F_1+1)/(F_1+1)/(2*F_1+3))^
(1/2)*((F_1-m_2)*(F_1+1-m_2)/(2*F_1+1)/(F_1+1))^(1/2);
```

$$Cgil(1,-1) := \frac{1}{48}\,(-1)^{2\,I\_nuc+2\,F\_1}$$

$$+1\sqrt{12\,F\_1+6}\,\sqrt{6}\,\left(\right.$$

$$-\frac{1}{(2\,F\_1+1)\,(F\_1+1)\,(2\,F\_1+3)}\left((2\,I\_nuc+2\,F\_1+5)\,(2\,I\_nuc\right.$$

$$\left.\left.+2\,F\_1+1)\,(2\,I\_nuc-2\,F\_1+1)\,(2\,I\_nuc-2\,F\_1-3)\right)\right)$$

$$^{1/2}\sqrt{\frac{(F\_1-m\_2)\,(F\_1+1-m\_2)}{(2\,F\_1+1)\,(F\_1+1)}}$$

```
> Cgil(1,0):=1/24*(-1)^(2*I_nuc+2*F_1+1)*(12*F_1+6)^(1/2)*
6^(1/2)*(-(2*I_nuc+2*F_1+5)*(2*I_nuc+2*F_1+1)*(2*I_nuc-2*
F_1+1)*(2*I_nuc-2*F_1-3)/(2*F_1+1)/(F_1+1)/(2*F_1+3))^
(1/2)*((F_1+1+m_2)*(F_1+1-m_2)/(2*F_1+1)/(F_1+1))^(1/2);
```

$$Cgil(1,0) := \frac{1}{24}\,(-1)^{2\,I\_nuc+2\,F\_1}$$

$$+1\sqrt{12\,F\_1+6}\,\sqrt{6}\,\left(\right.$$

$$-\frac{1}{(2\,F\_1+1)\,(F\_1+1)\,(2\,F\_1+3)}\left((2\,I\_nuc+2\,F\_1+5)\,(2\,I\_nuc\right.$$

$$\left.\left.+2\,F\_1+1)\,(2\,I\_nuc-2\,F\_1+1)\,(2\,I\_nuc-2\,F\_1-3)\right)\right)$$

$$^{1/2}\sqrt{\frac{(F\_1+1+m\_2)\,(F\_1+1-m\_2)}{(2\,F\_1+1)\,(F\_1+1)}}$$

```
> Cgil(1,1):=1/48*(-1)^(2*I_nuc+2*F_1+1)*(12*F_1+6)^(1/2)*
6^(1/2)*(-(2*I_nuc+2*F_1+5)*(2*I_nuc+2*F_1+1)*(2*I_nuc-2*
F_1+1)*(2*I_nuc-2*F_1-3)/(2*F_1+1)/(F_1+1)/(2*F_1+3))^
(1/2)*((F_1+m_2)*(F_1+1+m_2)/(2*F_1+1)/(F_1+1))^(1/2);
```

$$Cgil(1,1) := \frac{1}{48}\,(-1)^{2\,I\_nuc+2\,F\_1}$$

$$+1\sqrt{12\,F\_1+6}\,\sqrt{6}\left(-\frac{1}{(2\,F\_1+1)\,(F\_1+1)\,(2\,F\_1+3)}\left((2\,I\_nuc+2\,F\_1+5)\,(2\,I\_nuc+2\,F\_1+1)\,(2\,I\_nuc-2\,F\_1+1)\,(2\,I\_nuc-2\,F\_1-3)\right)\right)^{1/2}\sqrt{\frac{(F\_1+m\_2)\,(F\_1+1+m\_2)}{(2\,F\_1+1)\,(F\_1+1)}}$$

```
> ccoeff(4,3,3,2,7/2);
  # Just a test
```

$$-\frac{1}{8}\sqrt{6}\,\sqrt{7}$$

Calculations

Amplitudes (define amplitudes for rate calculations)

```
> m1:=F1; m2:=F2;
```

$$m1 := \frac{11}{2}$$

$$m2 := \frac{11}{2}$$

```
> E1st:= (F1,F2,m1,m2) -> alpha*(Estark.eps)*delta(F1,F2)*
  delta(m1,m2) + ccoeff(F1,F2,m1,m2,Inuc)*beta*(Estark &x
  eps).(I*z*delta(m1,m2) + (I*x-y)*delta(m1,m2+1) - (I*x+y)*
  delta(m1,m2-1));
```

$$E1st := (F1, F2, m1, m2) \rightarrow \alpha\, Estark.eps\,\delta(F1, F2)\,\delta(m1, m2) + (ccoeff(F1, F2, m1, m2, Inuc)\,\beta\, LinearAlgebra\text{-}\&x(Estark, eps)).(\mathrm{I}\,z\,\delta(m1, m2) + (\mathrm{I}\,x - y)\,\delta(m1, m2+1) - (\mathrm{I}\,x + y)\,\delta(m1, m2-1))$$

```
> Bterm:=(F1,F2,m1,m2) -> ccoeff(F1,F2,m1,m2,Inuc)*B.(z*delta
  (m1,m2) + (x+I*y)*delta(m1,m2+1) + (-x+I*y)*delta(m1,m2-1))
  ;
```

$$Bterm := (F1, F2, m1, m2) \rightarrow (ccoeff(F1, F2, m1, m2, Inuc)\,B).(z\,\delta(m1, m2) + (x + \mathrm{I}\,y)\,\delta(m1, m2+1) + (-x + \mathrm{I}\,y)\,\delta(m1, m2-1))$$

```
>
> M1rel:= Mrel*Bterm; M1hf:= Mhf*Bterm;
```

$$M1rel := 0.0002305\, Bterm$$

$$M1hf := 0.$$

```
> M1:= (F1,F2,m1,m2) -> ccoeff(F1,F2,m1,m2,Inuc)*(M1rel(F1,
  F2,m1,m2)+M1hf(F1,F2,m1,m2))*B.(z*delta(m1,m2) + (x+I*y)*
  delta(m1,m2+1) + (-x+I*y)*delta(m1,m2-1));
```

$$M1 := (F1, F2, m1, m2) \rightarrow (ccoeff(F1, F2, m1, m2, Inuc)\,(M1rel(F1, F2, m1, m2) + M1hf(F1, F2, m1, m2))\,B).(z\,\delta(m1, m2) + (x + \mathrm{I}\,y)\,\delta(m1, m2+1) + (-x$$

$$+ \mathrm{I}\,y)\,\delta(m1, m2-1)\big)$$

```
>
> E1pv:= (F1,F2,m1,m2) -> ccoeff(F1,F2,m1,m2,Inuc)*(I*Im
  (Epv)*eps.(z*delta(m1,m2) + (x+I*y)*delta(m1,m2+1) + (-x+I*
  y)*delta(m1,m2-1)));
```

$$E1pv := (F1, F2, m1, m2) \rightarrow ccoeff(F1, F2, m1, m2, Inuc)\ (\mathrm{I}\,\Im(Epv)\ eps).\big(z\,\delta(m1, m2) + (x + \mathrm{I}\,y)\,\delta(m1, m2+1) + (-x + \mathrm{I}\,y)\,\delta(m1, m2-1)\big)$$

Rate calculations

```
> W_E1st:= simplify(expand(E1st*conjugate(E1st)*tau));
```

$$W\_E1st := 2.203495201\ 10^{9}\ |E1st|^2$$

```
> W_M1rel:=simplify(expand(M1rel*conjugate(M1rel)*tau));
  W_M1hf:=simplify(expand(M1hf*conjugate(M1hf)*tau)); W_M1:=
  simplify(expand(M1*conjugate(M1)*tau));
```

$$W\_M1rel := 117.0722509\ |Bterm|^2$$

$$W\_M1hf := 0.$$

$$W\_M1 := 2.203495201\ 10^{9}\ |M1|^2$$

```
>
> Wsum_E1st_M1:= simplify(expand((E1st+M1)*conjugate(E1st+M1)
  *tau));
```

$$Wsum\_E1st\_M1 := 2.203495201\ 10^{9}\ E1st\ \underline{E1st} + 2.203495201\ 10^{9}\ E1st\ \underline{M1} + 2.203495201\ 10^{9}\ M1\ \underline{E1st} + 2.203495201\ 10^{9}\ M1\ \underline{M1}$$

```
> Wsub_E1st_M1:= simplify(expand((E1st-M1)*conjugate(E1st-M1)
  *tau));
```

$$Wsub\_E1st\_M1 := 2.203495201\ 10^{9}\ E1st\ \underline{E1st} - 2.203495201\ 10^{9}\ E1st\ \underline{M1} - 2.203495201\ 10^{9}\ M1\ \underline{E1st} + 2.203495201\ 10^{9}\ M1\ \underline{M1}$$

```
>
> E1st_M1_IFsignal:= Wsum_E1st_M1 - Wsub_E1st_M1;
```

#the E1-M1 IF signal asymmetry deltaR/R. Note: in Gilbert's thesis, she plots 1/4 * deltaR/R

$$E1st\_M1\_IFsignal := 4.406990402\ 10^{9}\ E1st\ \underline{M1} + 4.406990402\ 10^{9}\ M1\ \underline{E1st}$$

```
> E1st_M1_asymmetry:= E1st_M1_IFsignal/((Wsum_E1st_M1 +
  Wsub_E1st_M1)/2);
```

$$E1st\_M1\_asymmetry := \frac{4.406990402\ 10^{9}\ E1st\ \underline{M1} + 4.406990402\ 10^{9}\ M1\ \underline{E1st}}{2.203495200\ 10^{9}\ E1st\ \underline{E1st} + 2.203495200\ 10^{9}\ M1\ \underline{M1}}$$

Upcoming

Appendix B

DIFFERENTIAL AMPLIFIER FOR SATURATION SPECTROSCOPY AND DAVLL

The photodiode signals from the saturation spectroscopy and the DAVLL setups require subtraction of two signals. A differential amplifier for current sources is employed, based on a design that has been used in the Orozco group at the State University of New York at Stony Brook. One input channel has a separate gain adjustment so that the relative signal size can be adjusted (to compensate for different photodiode sensitivities etc.). After subtracting the two signals, a bias voltage can be applied to offset the signal and the overall gain of the difference signal can be set as well. Two outputs are available, one has typically a low-pass filter to cut higher frequency noise.

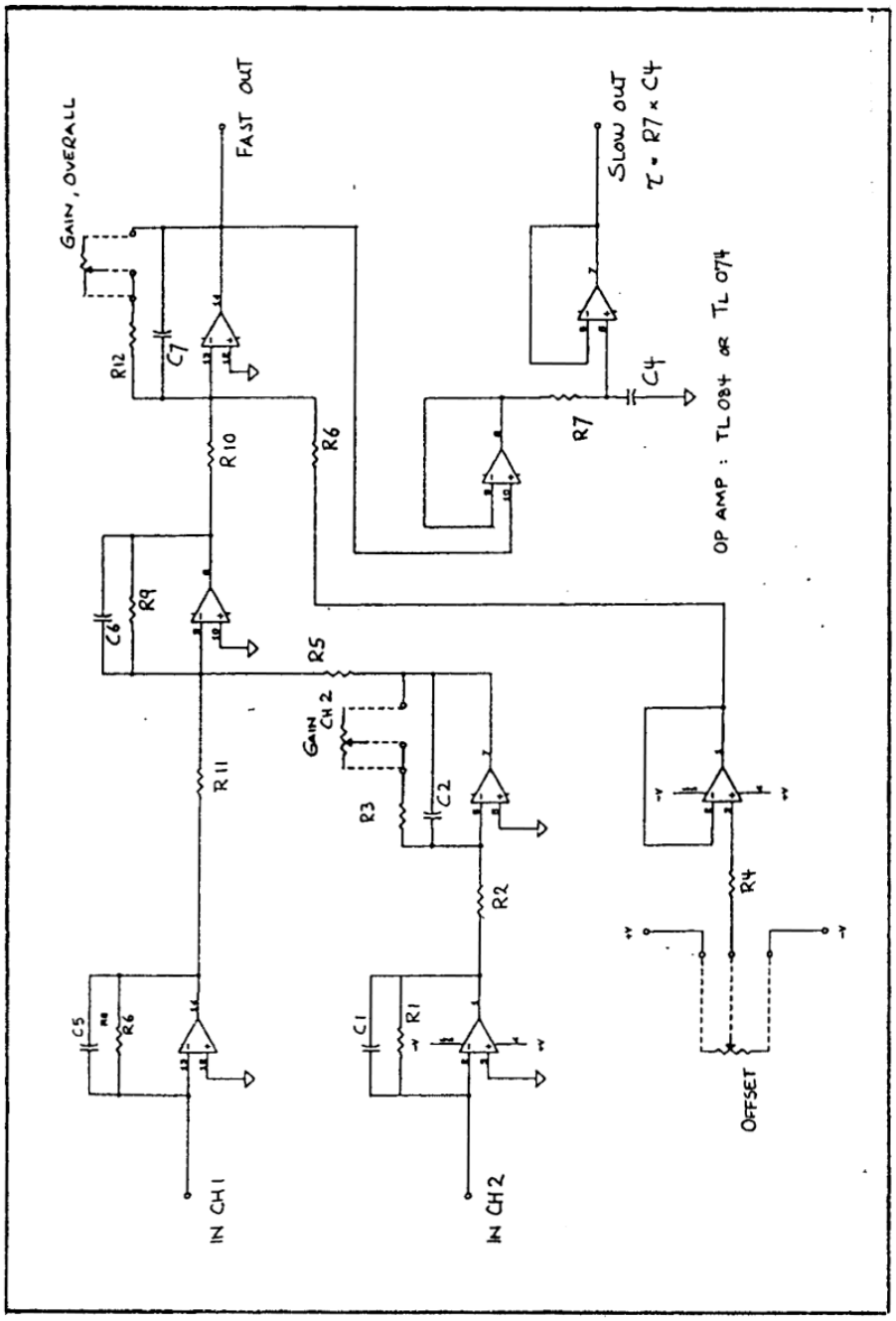

Figure B.1: Circuit diagram of the differential amplifier used for saturation spectroscopy and DAVLL.

Component	**Value**
U1, U2	TL074
R1, R8	47 k
R2, R5, R6, R11, R10, R12	4.7 k
R7	20 k
R3	3 k
R4	10 k
C1, C2, C5, C6	68 p
C4	10 n
at all V+/- pins	100 n to GND
V+	15 V
V-	15 V
Gain, overall	50 k
Gain, ch2	10 k
Offset	5 k

Table B.1: Components and their values for the differential amplifier circuit.

BIBLIOGRAPHY

[1] I. M. Savukov, A. Derevianko, H. G. Berry, W. R. Johnson. Large Contributions of Negative-Energy States to Forbidden Magnetic-Dipole Transition Amplitudes in Alkali-Metal Atoms. Physical Review Letters, V. 83, N. 15, 11 October, 1999.

[2] Question of Parity Conservation in Weak Interactions. Physical review [0031-899X] LEE. Year: 1956 vol: 104 iss: 1 pg: 254 - 258

[3] Weinberg, S. (1967). Phys. Rev. Lett., 19, 1264; (1972), Phys. Rev., 5D, 1412

[4] Glashow, Sh. L. (1961). Nucl. Phys., 22, 579.

[5] V. V. Flambaum and D. W. Murray. Anapole moment and nucleon weak interactions. Phys. Rev. C, 56:1641, 1997.

[6] Zel'dovich, Ya. B. (1959). ZhETF, 36, 964 (Sov. Phys. JETP, 9, 682)

[7] Observation of parity nonconservation in atomic transitions. JETP letters [0021-3640]. Barkov, L.M., and Zolotorev, M. S.. yr: 1978, vol: 27, iss: 6, pg: 357-361.

[8] Preliminary Observation of Parity Nonconservation in Atomic Thallium. R. Conti, P. Bucksbaum, S. Chu, E. Commins, and L. Hunter. Phys. Rev. Lett. vol: 42, number: 6, pages: 343-346, year: 1979, month: Feb.

[9] M.A. Bouchiat and C. Bouchiat. Parity Violation Induced by Weak Neutral Currents in Atomic Physics. Part I. Le Journal de Physique. 1974

[10] C.S. Wood, S.C. Bennett, D. Cho, B.P. Masterson, J.L. Roberts, C.E. Tanner, C.E. Wieman, Science 275, 1759 (1997)

[11] Observation of a Large Atomic Parity Violation Effect in Ytterbium.

[12] Possibility of measuring parity non-conservation with a single trapped atomic ion, N. Fortson, Phys. Rev. Lett. 70, 2383-2386 (1993).

[13] Radio frequency spectroscopy with a trapped Ba+ ion: recent progress and prospects for measuring parity violation, T. W. Koerber, M. H. Schacht, W. Nagourney, and E. N. Fortson, J. Phys. B. 36, 637-648 (2003).

[14] A recent poster about the experiments of Parity Non-Conservation in Nuclei by the DeMille group:
`http://www.yale.edu/demillegroup/posters/anapole-poster.pdf`

[15] Experimental study of vapor-cell magneto-optical traps for efficient trapping of radioactive atoms. The European physical journal. D, Atomic, molecular and optical physics [1434-6060] Atutov. yr: 2009 vol: 53 iss: 1 pg: 89 - 96

[16] Fundamental symmetries studies with cold trapped francium atoms at ISAC. Hyperfine interactions [0304-3843] Gwinner. yr: 2006 vol: 172 iss: 1-3 pg: 45 - 51

[17] I. B. Khriplovich. Parity Non-Conservation in Atomic Phenomena. Gordon and Breach, New York, 1991.

[18] Salam, A. (1968). In Proceedings of the 8th Nobel Symposium. New York: J. Wiley

[19] M.A. Bouchiat and C. Bouchiat. Parity Violation Induced by Weak Neutral Currents in Atomic Physics. Part II. Le Journal de Physique. 1975.

[20] B. H. Bransden and C. J. Joachain. Physics of Atoms and Molecules. Longman Inc., New York, 1983.

[21] Charles H. Townes, Arthur L. Schawlow. Microwave Spectroscopy. Courier Dover Publications, 1975.

[22] J.S.M. Ginges, V.V. Flambaum. Physics Reports 398 (2004) 63-154

[23] J.M.W. Krüger. A Novel Technique for Frequency Stabilizing Laser Diodes. University of Otago. October, 1998.

[24] S. Gilbert. Parity violation in atomic cesium and associated experiments. PhD thesis, University of Michigan, 1984.

[25] Precision measurement of parity nonconservation in cesium. C.S. Wood, S.C. Bennett, J.L. Roberts, D. Cho, and C.E. Wieman.1 JILA, University of Colorado and National Institute of Standards and Technology, and Department of Physics, University of Colorado, Boulder, CO 80309-0440, U.S.A.

[26] V. A. Dzuba, V. V. Flambaum, and O. P. Sushkov. Calculation of energy levels, E1 transition amplitudes, and parity violation in francium. Phys. Rev. A, 51:3454, 1995.

[27] M. S. Safronova and W. R. Johnson. High-precision calculation of the parity-nonconserving amplitude in francium. Phys. Rev. A, 62:022112, 2000.

[28] ZT Lu, C. Bowers, SJ Freedman, BK Fujikawa, JL Mortara, SQ Shang, KP Coulter, and L. Young. Laser trapping of short-lived radioactive isotopes. Physical Review Letters, 72, 3791 (1994).

[29] G. Gwinner, JA Behr, SB Cahn, A. Ghosh, LA Orozco, GD Sprouse, and F. Xu. Magneto-optic trapping of radioactive^{79} Rb. Physical Review Letters, 72, 3795 (1994).

[30] M. Stephens and C. Wieman. High collection efficiency in a laser trap. Physical review letters, 72, 3787 (1994).

[31] G. Gwinner. Laser trapping of radioactive atoms. PhD Thesis, SUNY Stony Brook, 1995.

[32] C. Monroe, W. Swann, H. Robinson, and C. Wieman. Very cold trapped atoms in a vapor cell. Phys. Rev. Lett., 65:15711574, 1990.

[33] K. L. Corwin, Z.-T. Lu, C. F. Hand, R. J. Epstein, and C. E. Wieman. Frequency-Stabilized Diode Laser with the Zeeman Shift in an Atomic Vapor. Applied Optics, 37, 3295 (1998).

[34] C. E. Wieman and L. Hollberg. Using diode lasers for atomic physics. Review of Scientific Instruments, 62, 1 (1991).

[35] UMichigan internal report by K. Vogel, `http://cold-atoms.physics.lsa.umich.edu/education/REU/2004/kevin.vogel/DAVLLsetup.pdf`, accessed July 2010.